iScience

CellPress
OPEN ACCESS

Article

Retinal Degeneration Caused by Rod-Specific *Dhdds* Ablation Occurs without Concomitant Inhibition of Protein *N*-Glycosylation

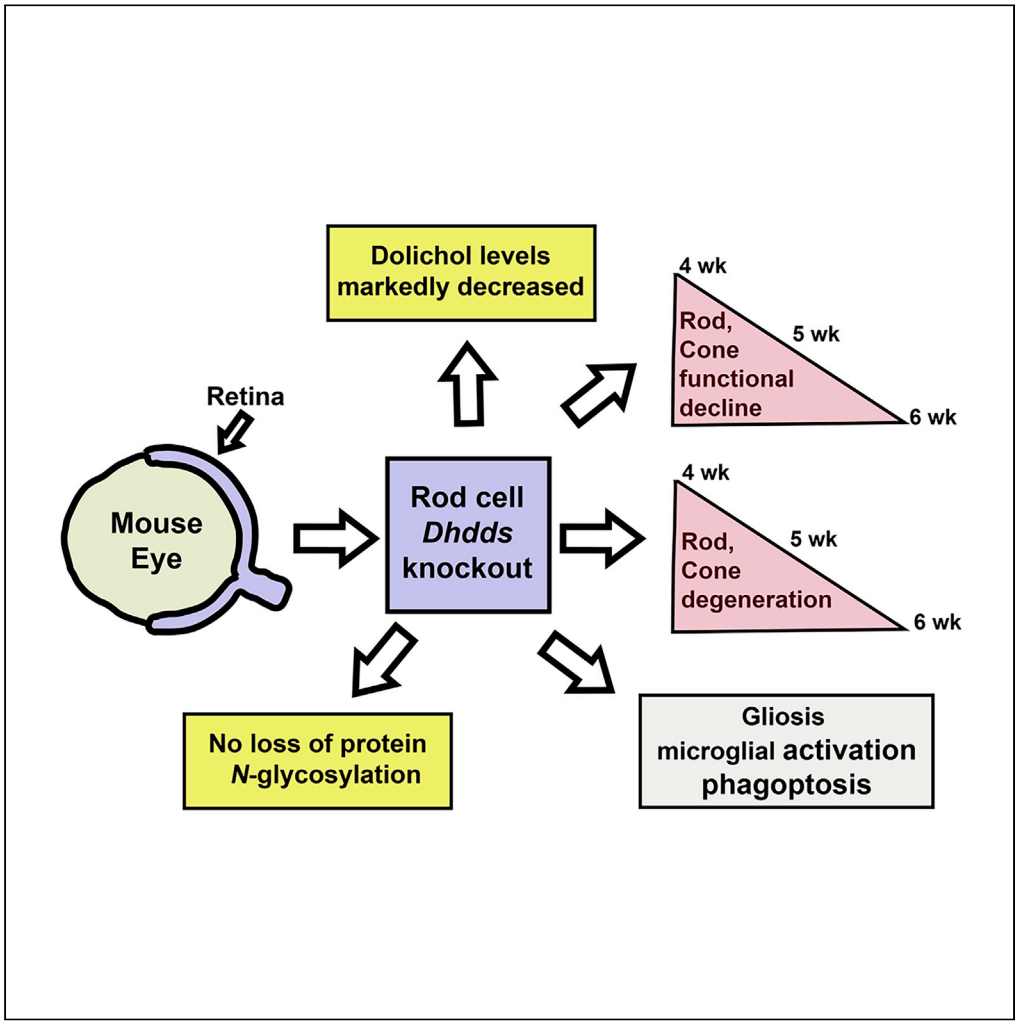

Sriganesh Ramachandra Rao, Lara A. Skelton, Fuguo Wu, ..., Ewa Swiezewska, Steven J. Pittler, Steven J. Fliesler

fliesler@buffalo.edu

HIGHLIGHTS

Deletion of *Dhdds* in rod cells caused rapid retinal degeneration in mice

Retinal dolichol levels markedly decreased before onset of degeneration

Protein *N*-glycosylation was uncompromised despite *Dhdds* deletion

Degeneration also involved gliosis, microglial activation, and phagoptosis

Ramachandra Rao et al., iScience *23*, 101198
June 26, 2020
https://doi.org/10.1016/j.isci.2020.101198

iScience

CellPress
OPEN ACCESS

Article

Retinal Degeneration Caused by Rod-Specific *Dhdds* Ablation Occurs without Concomitant Inhibition of Protein *N*-Glycosylation

Sriganesh Ramachandra Rao,[1,2,3] Lara A. Skelton,[1,2,3] Fuguo Wu,[1,3,4] Agnieszka Onysk,[5] Grzegorz Spolnik,[7] Witold Danikiewicz,[7] Mark C. Butler,[1,2,8] Delores A. Stacks,[6] Liliana Surmacz,[5] Xiuqian Mu,[1,3,4] Ewa Swiezewska,[5] Steven J. Pittler,[6] and Steven J. Fliesler[1,2,3,9,*]

SUMMARY

Dehydrodolichyl diphosphate synthase (DHDDS) catalyzes the committed step in dolichol synthesis. Recessive mutations in *DHDDS* cause retinitis pigmentosa (RP59), resulting in blindness. We hypothesized that rod photoreceptor-specific ablation of *Dhdds* would cause retinal degeneration due to diminished dolichol-dependent protein *N*-glycosylation. *Dhdds*$^{flx/flx}$ mice were crossed with rod-specific Cre recombinase-expressing (Rho-iCre75) mice to generate rod-specific *Dhdds* knockout mice (*Dhdds*$^{flx/flx}$ iCre^{+}). *In vivo* morphological and electrophysiological evaluation of *Dhdds*$^{flx/flx}$ iCre^{+} retinas revealed mild retinal dysfunction at postnatal (PN) 4 weeks, compared with age-matched controls; however, rapid photoreceptor degeneration ensued, resulting in almost complete loss of rods and cones by PN 6 weeks. Retina dolichol levels were markedly decreased by PN 4 weeks in *Dhdds*$^{flx/flx}$ iCre^{+} mice, relative to controls; despite this, *N*-glycosylation of retinal proteins, including opsin (the dominant rod-specific glycoprotein), persisted in *Dhdds*$^{flx/flx}$ iCre^{+} mice. These findings challenge the conventional mechanistic view of RP59 as a congenital disorder of glycosylation.

INTRODUCTION

Retinitis pigmentosa (RP) represents a large class of inherited retinal dystrophies caused by mutations in several families of genes, leading to pigmentary retinopathy and progressive, irreversible blindness. Typically, RP is characterized by the initial loss of rod photoreceptors (PRs), deposition of pigment granules, and peripheral vision loss (Ferrari et al., 2011; Hamel, 2006). Defective asparagine-linked glycosylation (*N*-glycosylation) of proteins in rod cells, particularly the visual pigment rhodopsin (RHO), results in progressive, irreversible rod cell degeneration and death, with concomitant loss of vision (Murray et al., 2009, 2015; Kaushal et al., 1994; Fliesler et al., 1984a). Successful glycosylation of RHO is necessary for its vectorial trafficking through the inner segment (cell body) of the rod cell to the site of rod outer segment (ROS) membrane assembly at the base of the ROS. Retinal degeneration has been observed in patients harboring RHO mutations involving the *N*-glycosylation consensus sites, and in animal models involving comparable RHO mutations (Van Den Born et al., 1994, Zhu et al., 2004; Sullivan et al., 1993; Murray et al., 2015; Iwabe et al., 2016), as well as by tunicamycin-induced and genetic inhibition of global/RHO *N*-glycosylation (Fliesler and Basinger, 1985; Fliesler et al., 1985; Sabry et al., 2016; Thompson et al., 2013; Murray et al., 2015). Protein *N*-glycosylation involves the following steps (schematic representation, Figure 1): generation of dolichol (Dol, an important isoprenoid arising from the mevalonate pathway) and dolichyl phosphate (Dol-P, the obligate glycan carrier necessary for *N*-linked glycosylation, *O*-mannosylation, and *C*-mannosylation) (Burda and Aebi, 1999; Endo et al., 2003; Park et al., 2014; Cantagrel et al., 2010; Burton et al., 1979; Maeda et al., 2000; Doucey et al., 1998), generation of complex Dol-P-linked oligosaccharides (DLO) (Krasnova and Wong, 2016; Gandini et al., 2017; Behrens and Leloir, 1970), and transfer of those oligosaccharides from DLO to the *N*-glycosylation consensus site on the target polypeptide (Welply et al., 1983). Genetic defects affecting the glycosylation mechanism constitute a large family of syndromes termed "congenital disorders of glycosylation" (CDGs), with more than 150 causative genes (Ng and Freeze, 2018; Sparks and Krasnewich, 1993). A family of genetic diseases pertaining to Dol synthesis is classified as CDG-I (the class of CDG involving defective glycan assembly and/or their transfer in the endoplasmic reticulum [ER]) due to

[1]Department of Ophthalmology/Ross Eye Institute, Jacobs School of Medicine and Biomedical Sciences, State University of New York- University at Buffalo, Buffalo, NY 14209, USA

[2]Research Service, VA Western NY Healthcare System, Buffalo, NY 142015, USA

[3]Department of Biochemistry, Jacobs School of Medicine and Biomedical Sciences, State University of New York- University at Buffalo, Buffalo, NY 14203, USA

[4]New York State Center of Excellence in Bioinformatics and Life Sciences, State University of New York-University at Buffalo, Buffalo, NY 14203, USA

[5]Institute of Biochemistry and Biophysics, Polish Academy of Sciences, Warsaw, Poland

[6]Department of Optometry and Vision Science, Vision Science Research Center, School of Optometry, University of Alabama at Birmingham, Birmingham, AL 35294, USA

[7]Institute of Organic Chemistry, Polish Academy of Sciences, Warsaw 02106, Poland

[8]Present address: Custom Collaborators LLC, Clarence Center, NY 14051, USA

[9]Lead Contact

*Correspondence: fliesler@buffalo.edu

https://doi.org/10.1016/j.isci.2020.101198

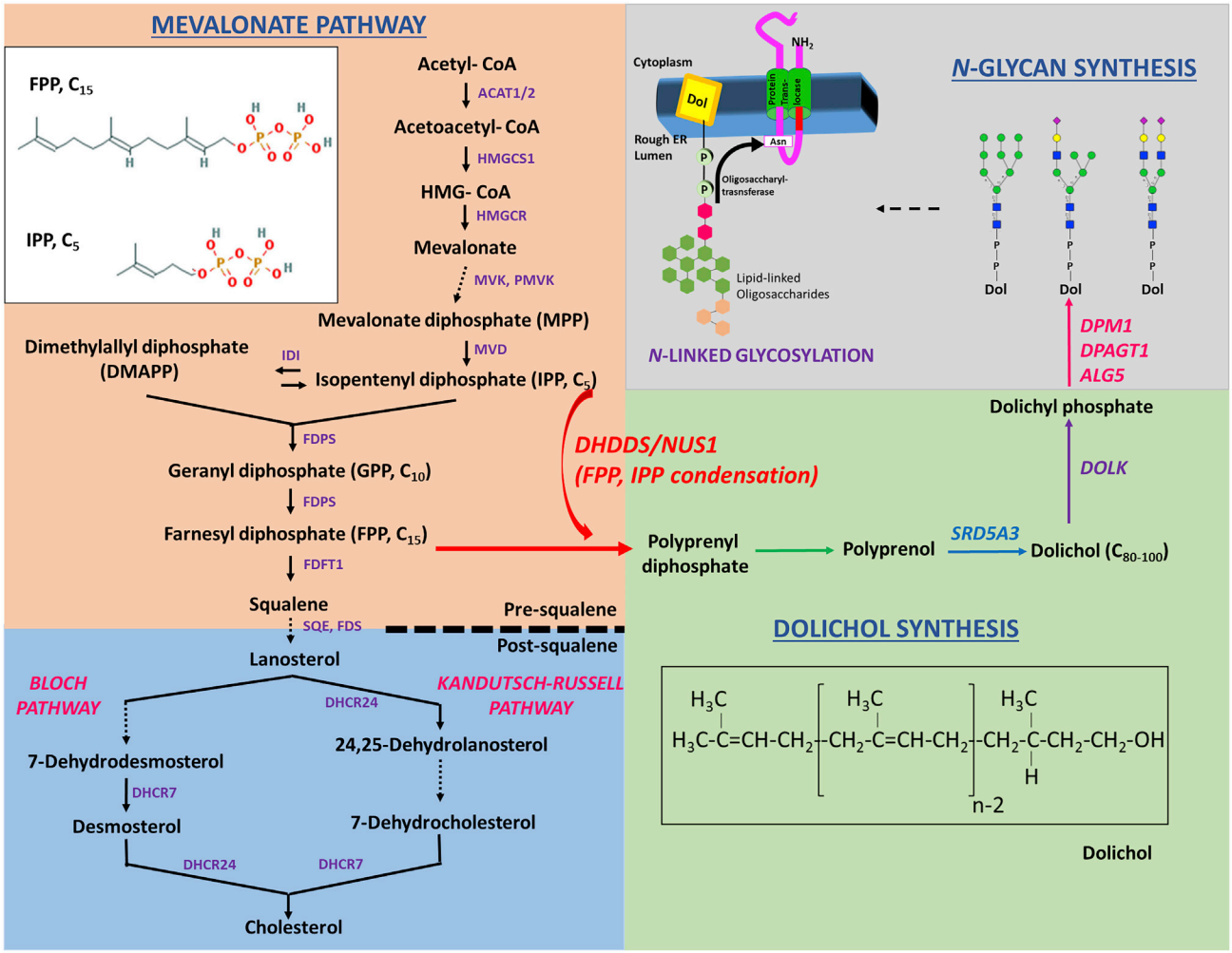

Figure 1. Schematic Representation of the Mevalonate Pathway, Dolichol Synthesis, and the Requirement of Dolichyl Phosphate (Dol-P) for N-Linked Oligosaccharide Generation

Farnesyl diphosphate (FPP), an important pre-squalene intermediate of the mevalonate pathway, undergoes DHDDS/NUS1-catalyzed condensation with multiple isopentenyl pyrophosphate (IPP) units to generate polyprenyl pyrophosphate (diphosphate), and ultimately the obligate glycan carrier, Dol-PP. Gene products involved in synthesis of dolichol and Dol-P-saccharide/oligosaccharide intermediates, and hence implicated in CDG-1 (Congenital Disorders of Glycosylation), have been represented. The enzymatic activity provided by DHDDS and NUS1 catalyzes the commitment step of dolichol synthesis; hence mutations in either DHDDS or NUS1 are hypothesized to block protein N-glycosylation, and are classified as CDG-I. Dolichol (*structure in inset*), is an acyclic isoprenoid consisting of 18–21 isoprene units.

the requirement of DLO for *N*-glycosylation. Common clinical features of CDGs include failure to thrive, retarded development, protein-losing enteropathy, early-onset encephalopathy, as well as retinopathies such as RP (Sparks and Krasnewich, 1993; Thompson et al., 2013; Hamdan et al., 2017; Morava et al., 2009).

Two key intermediate metabolites in the mevalonate pathway, farnesyl pyrophosphate (FPP; also called farnesyl diphosphate) and isopentenyl pyrophosphate (IPP; also called isopentyl diphosphate), serve as precursors for squalene, cholesterol, and Dol synthesis (see Figure 1) (Grabowska et al., 1998). The committed enzymatic step in the pathway toward Dol synthesis is the catalytic condensation of FPP with multiple IPP molecules to form polyprenyl diphosphate; this reaction is catalyzed by a *cis*-prenyltransferase (CPT) complex composed of dehydrodolichyl diphosphate synthase (DHDDS) and Nogo-B receptor (NgBR; gene symbol *NUS1*) (Park et al., 2014). Polyprenyl diphosphate sequentially undergoes dephosphorylation (action of dolichyl diphosphate phosphatase 1 [DOLPP1]) (Rush et al., 2002), reduction (action of steroid Δ5 *alpha*-reductase 3 [SRD5A3]) (Cantagrel et al., 2010), and phosphorylation (action of dolichol kinase [DOLK]) (Shridas and Waechter, 2006) to generate Dol-P (Schenk et al., 2001). Cellular *de novo* synthesis

and availability of Dol-P in the ER (Heesen et al., 1994; Wu et al., 2003; Ashida et al., 2006) are necessary for DLO-dependent protein glycosylation (Jakobsson et al., 1989). Genetic defects affecting Dol-P *de novo* synthesis at the level of DHDDS, NgBR, SRD5A3, or DOLK are classified within the CDG-1 subgroup of CDGs (Sparks and Krasnewich, 1993; Park et al., 2014).

Heretofore, animal model or *in vitro* studies have employed approaches such as inhibition of the Dol-P-dependent oligosaccharyltransferase (OST, e.g., using tunicamycin) (Fliesler et al., 1984a, 1984b, 1985; Fliesler and Basinger, 1985) or mutation of the glycosylation consensus sites on specific target proteins (e.g., rhodopsin; Murray et al., 2015) to evaluate the requirement of protein *N*-glycosylation in the retina. Herein, we addressed this requirement by genetic blockade of the rate-limiting step in dolichol synthesis, i.e., the *cis*-prenyltransferase (CPT) activity of DHDDS.

Recent studies involving genetic screening of families with a rare autosomal recessive form of retinitis pigmentosa (RP59) demonstrated a founder missense mutation (K42E) in the *DHDDS* gene (Zelinger et al., 2011; Zuchner et al., 2011). Two other rare, pathogenic *DHDDS* mutations (T206A, R98W), both found heterozygously with the K42E mutation, also have been reported (Wen et al., 2013; Biswas et al., 2017; Kimchi et al., 2018). In patients homozygous for the K42E mutation, the peripheral retina underwent thinning, but the cone-rich fovea is well-preserved. Functionally, in one patient examined, dark-adapted ("scotopic," rod-driven) electroretinogrphic (ERG) responses were extinguished by 21–24 years of age, leading to a visual field limited to a small central island, consistent with rod-cone dystrophy or early-onset retinal degeneration. In an infant presenting as a compound heterozygote (W64X and p.Cys148GlufsX11), ERG responses were undetectable at 2 months of age, but the patient died at 7 months of age from multiple systemic complications due to insufficient DHHDS activity (Sabry et al., 2016), and thus is distinctly different from the K42E phenotype. The mutations in the *"severe"* phenotype infant led to loss of FPP/IPP-binding sites, much similar to the excision of *Dhdds* Exon 3 used in the current study (see Figures S1 and S2; Sabry et al., 2016). Retinal degeneration also has been observed in patients of Romani origin harboring mutations in the gene coding for the DHDDS-heterodimeric partner NgBR (Park et al., 2014). The pathological mechanisms and defective cell processes attributed to RP59, although currently hypothesized to be hypoglycosylation driven, remain to be directly tested. This is largely due to the lack of a validated vertebrate animal model of RP59 to evaluate the link between mammalian *cis*-prenyltransferase DHDDS activity, its requirement for protein *N*-glycosylation, and the establishment and preservation of normal retinal structure and function. Up until recently, only a zebrafish *Dhdds* knockdown model has been reported (Wen et al., 2014; Zuchner et al., 2011). However, more recently, a report of a K42E knock-in mouse model was published (Ramachandra Rao et al., 2020), but dolichol levels and *cis*-prenyltransferase activity were not examined.

Given this information, we hypothesized that PR-specific deletion of *Dhdds* would elicit a primary PR degeneration owing to the critical requirement of protein *N*-glycosylation for maintenance of PR structure, function, and viability. In the current study, we generated a novel murine, rod PR-specific *Dhdds* knockout model on a C57BL/6J background and examined the functional, morphological, and biochemical consequences to the retina. Contrary to expectation, although a profound retinal degeneration was observed, we found no evidence for defective protein *N*-glycosylation in this mouse model, despite confirmed ablation of *Dhdds* in essentially the entire population of retinal rod cells.

RESULTS

Verification of Rod Photoreceptor-Specific Dhdds Deletion

A graphical representation of the genotyping strategy utilized for the verification of $Dhdds^{flx/flx}$ $iCre^{+}$ mice is provided in Figures S4, 2A, and 2B. Exon 3, coding for critical FPP- and IPP-binding sites, was chosen for targeted deletion (Figures S2 and S3). Initially, tail snip genotyping analysis was performed to detect floxed *Dhdds* allele and Rho-iCre transgenes: *Dhdds* allele with *loxP* modification and wild-type (WT) *Dhdds* allele yielded 393-bp and 517-bp PCR products, respectively (Figures S4A and S4C). Similarly, Rho-iCre transgene yielded a 650-bp PCR product, as shown previously (Figure S4B) (Li et al., 2005). To further validate excision of the floxed *Dhdds* allele in rod PRs, genomic DNA extracted from $Dhdds^{flx/flx}$ $iCre^{-}$ (lanes 2, 4, 6 in Figure 2C) and $Dhdds^{flx/flx}$ $iCre^{+}$ retinas (lanes 1, 3, 5 in Figure 2C) (n = 3/group) (already verified by tail snip genotyping as demonstrated in Figure S4A and S4B) was subjected to PCR amplification using intronic primers designed upstream and downstream of the targeted exon (see Figures 2B and S4C). Genomic material from tail snip genotype-verified $Dhdds^{flx/flx}$ $iCre^{+}$ retinas yielded a 650-bp PCR product for Cre recombinase, as previously reported (Li et al., 2005) (top panel, Figure 2C), as well as a 584-bp

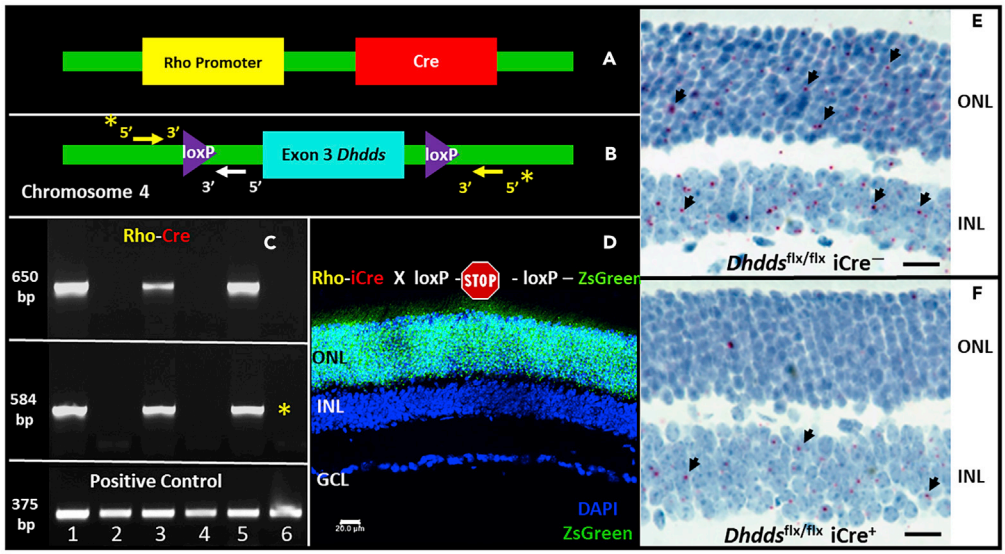

Figure 2. Verification of Rod Photoreceptor-Specific Deletion of *Dhdds*

(A–E) Rod-specific ablation of *Dhdds* was achieved by generating a mouse model harboring homozygous *loxP* sites flanking *Dhdds* exon 3 (gene locus: murine chromosome 4, 66.47 cM] (A) and cross-breeding against a transgenic mouse line consisting of opsin promoter-driven Cre recombinase (Rho-iCre75, (B)). The cross ultimately generated the knockout line of interest: *Dhdds*$^{flx/flx}$ iCre^{+}. *Dhdds*$^{flx/flx}$ iCre^{+} mice were first identified using tail snip genotyping (see also Figure S4). To verify photoreceptor-specific gene excision, whole retinas harvested from mice identified as *Dhdds*$^{flx/flx}$ iCre^{+} and age-matched WT controls were subjected to direct tissue genotyping (C, see also Figure S4 for primer design strategy). Retinas from *Dhdds*$^{flx/flx}$ iCre^{+} mice yielded short PCR product (584 bp, *upper panel*, (C) corresponding to the flanking intronic region only (*white arrow*, B), while positive for Rho-iCre transgene (*middle panel*, C). Control retinal tissue, negative for Cre recombinase (*upper panel*, C), did not exhibit excision of exon 3 (*middle panel*, C). PCR reaction against a housekeeping gene (*Dhcr7*) demonstrates intact genomic content in all biological samples (*bottom panel*, C). Direct tissue genotyping targeting Cre recombinase does not provide morphological context regarding its expression or activity. Rho-iCre75 line was crossed with a ZsGreen reporter mouse: a representative confocal micrograph (D) shows ZsGreen expression exclusively in majority of cells (overwhelmingly rods) in the photoreceptor layer at PN 4 weeks (scale bar, 20 μm). *In situ hybridization* with a probe corresponding to exon 3 of *Dhdds* suggests successful ablation of *Dhdds* in *Dhdds*$^{flx/flx}$ iCre^{+} mice (F), when compared with *Dhdds*$^{flx/flx}$ iCre^{-} mice (E). (Scale bars: 20 μm in (E and F)).

product that corresponds to the remnant intronic region upon excision of exon 3 (middle panel, Figure 2C) (see Methods for primer details, and Discussion for rationale). *Dhdds* WT allele (arising from other retinal cell types) would yield a predicted, larger (1.4 kbp) product (consisting of exon 3 as well as the flanking intronic regions) that is not amplified by a PCR protocol involving a short extension period of 45 s (See Methods) (Figures 2C and S4C). A non-specific, unaltered gene region (*Dhcr7*, 375-bp product) was PCR amplified as a positive control to verify genomic DNA quality (bottom panel, Figure 2C).

Rod PR-specific excision of *Dhdds* exon 3 is a function of spatiotemporal expression and activity of Cre recombinase (driven by the *Rho* promoter) (Li et al., 2005). Cre recombinase activity in Rho-iCre75 mice was verified using a reporter mouse strategy. Briefly, the Rho-iCre75 mouse line was crossed with a ZsGreen Ai6 reporter mouse line (harboring CAG artificial promoter-driven ZsGreen [variant of GFP]) with an upstream floxed transcriptional termination cassette (Figure 2D). Cell type/tissue-specific Cre activity, if present, relieves the ZsGreen transcription blockade by excising the upstream, loxP-modified transcription termination cassette, allowing ZsGreen expression. Retinas harvested from the first filial (F_1) generation of the Rho-iCre-ZsGreen Ai6 reporter mouse crossing at PN 15 days (Figure S5) and PN 30 days (*lower panel*, Figure 2D) were tested for rod-specific ZsGreen expression using laser confocal fluorescence microscopy. Representative fluorescence micrographs (Figure 2D) revealed ZsGreen expression in the vast majority of rod PR nuclei by PN 15 and PN 30 days, in good agreement with the published literature (Li et al., 2005).

Retinal expression of *Dhdds* transcript was directly tested utilizing customized BaseScope *in situ* hybridization (ISH) probes (two ZZ probes) designed against a murine *Dhdds* transcript region corresponding to coding exon 3 (bp 361–455 of NM_026144.4). A single mRNA transcript appears as single, red chromogenic

dot; bright-field images from ISH experiments in *Dhdds*$^{flx/flx}$ iCre^{+} and *Dhdds*$^{flx/flx}$ iCre^{-} mice (Figures 2E and 2F, respectively) suggest PR (outer nuclear layer [ONL])-specific loss of *Dhdds* transcript (tested at PN 30 days), whereas the adjacent inner nuclear layer (INL) retained a comparable level of ISH label as observed in WT control retinas.

Profound and Rapid Retinal Degeneration and Dysfunction Are Observed in Dhdds$^{flx/flx}$ iCre^{+} Mice

Age-matched *Dhdds*$^{flx/flx}$ iCre^{-} and *Dhdds*$^{flx/flx}$ iCre^{+} mice were subjected to *in vivo* retinal imaging and quantitative morphometric analysis using spectral domain optical coherence tomography (SD-OCT). ONL thickness was measured (in mm) around the optic nerve head. Figure 3A (left panel) shows a set of representative SD-OCT images of retinas from PN 5-week-old controls versus PN 4-, 5-, and 6-week-old *Dhdds*$^{flx/flx}$ iCre^{+} mice. ONL thickness values for PN 4-week-old *Dhdds*$^{flx/flx}$ iCre^{+} mice were comparable to those of control mice at PN 5 weeks of age (see Figure 3A, right panel). The ONL in the SD-OCT images appears as a hyporeflective region (demarcated by yellow dotted lines, Figure 3A, left panel). The ONL in *Dhdds*$^{flx/flx}$ iCre^{+} mice underwent significant thinning (*ca.* 50% compared with age-matched controls, $n = 4$, $p < 0.01$) by PN 5 weeks and was essentially absent by PN 6 weeks of age ($n = 4$, $p < 0.01$). A graphical comparison of ONL thickness (in mm) is provided in Figure 3A (right panel). The SD-OCT data correlate well with results obtained by conventional, paraffin-embedment histological analysis (see Figures S13A and S13B).

Scotopic ERG responses in *Dhdds*$^{flx/flx}$ iCre^{+} mice were diminished at all tested time points, relative to age-matched *Dhdds*$^{flx/flx}$ iCre^{-} controls (n = 7–12/group/time point) (Figure 3B). Scotopic a- and b-waves were recorded using a customized 16-step regimen over a range of flash intensities spanning 10^{-5} to 500 cd-s/m^2. The a-wave amplitude is a measure of PR hyperpolarization in response to photon flash stimulus. Scotopic a-wave amplitudes (at PN weeks 4, 5, and 6) were significantly lower, compared with those of age-matched controls, at all flash intensities $\geq$0.4 cd-s/m^2. Scotopic a-wave amplitudes in *Dhdds*$^{flx/flx}$ iCre^{+} mice at PN 4 weeks (n = 9) were significantly diminished at all flash intensities (~75% of the maximal control response amplitude [n = 12]). At PN 5 weeks of age (n = 12), a time point at which significant thinning of the ONL was observed, a-wave response amplitudes were significantly diminished (~35% of control values). The a-wave ERG responses in *Dhdds*$^{flx/flx}$ iCre^{+} were essentially extinguished by PN 6 weeks of age (n = 7) (Figure 3B, upper panel). A similar time-dependent, significant decrease was observed in scotopic b-wave responses of *Dhdds*$^{flx/flx}$ iCre^{+} mice, when compared with controls (Figure 3B, middle panel). Interestingly, b-wave response amplitudes were significantly reduced in all age groups of *Dhdds*$^{flx/flx}$ iCre^{+} mice compared with age-matched controls (for all flash intensities $\geq 10^{-3}$ cd-s/m^2), even at low flash intensities that may correspond to pure rod-mediated responses. Scotopic b-wave response amplitudes of *Dhdds*$^{flx/flx}$ iCre^{+} mice at PN 6 weeks of age (n = 7) exhibited about a 7-fold decrease compared with controls. Representative scotopic ERG traces for *Dhdds*$^{flx/flx}$ iCre^{+} mice and age-matched controls, at a saturating flash intensity of 500 cd-s/m^2, are provided in Figure S6. Under these conditions, whereas control responses were robust at all ages tested, the *Dhdds*$^{flx/flx}$ iCre^{+} mice exhibited diminishing response amplitudes, being nearly extinguished by PN 6 weeks.

Scotopic b:a wave amplitude ratios were significantly increased at PN 5 weeks of age in *Dhdds*$^{flx/flx}$ iCre^{+} mice at all flash intensities $\geq$0.4 cd-s/m^2, compared with age-matched controls. However, at PN 4 weeks of age, *Dhdds*$^{flx/flx}$ iCre^{+} mice showed increased scotopic b:a wave amplitude ratios only at flash intensities $\geq$150 cd-s/m^2 (Figure 3C, left panel). Also, implicit time values for scotopic b-wave were significantly elevated at both PN 4 and 5 weeks of age in *Dhdds*$^{flx/flx}$ iCre^{+} mice (Figure 3C, right panel), compared with age-matched controls.

In contrast, cone PR-driven (photopic) ERG responses (calculated as the difference between the photopic b-wave and a-wave maxima) in *Dhdds*$^{flx/flx}$ iCre^{+} mice at PN 4 and 5 weeks were comparable with those of age-matched controls at all flash intensities (ranging from 10^{-1} to 30 cd-s/m^2) (Figure 3B, bottom panel). However, photopic responses at PN 6 weeks of age were extinguished (n = 7) (i.e., equivalent to background noise levels), consistent with a rod-cone dystrophy (see Discussion).

Immunohistochemical (IHC) analysis of retinas from controls and *Dhdds*$^{flx/flx}$ iCre^{+} mice at PN 5 weeks (a time point at which structural and functional deficits in the retina were observed) with antibodies against rod opsin and glial fibrillary acidic protein (GFAP) suggested several key degenerative features. The GFAP immunoreactivity pattern demonstrated gliosis of the degenerating *Dhdds*$^{flx/flx}$ iCre^{+} retina (green

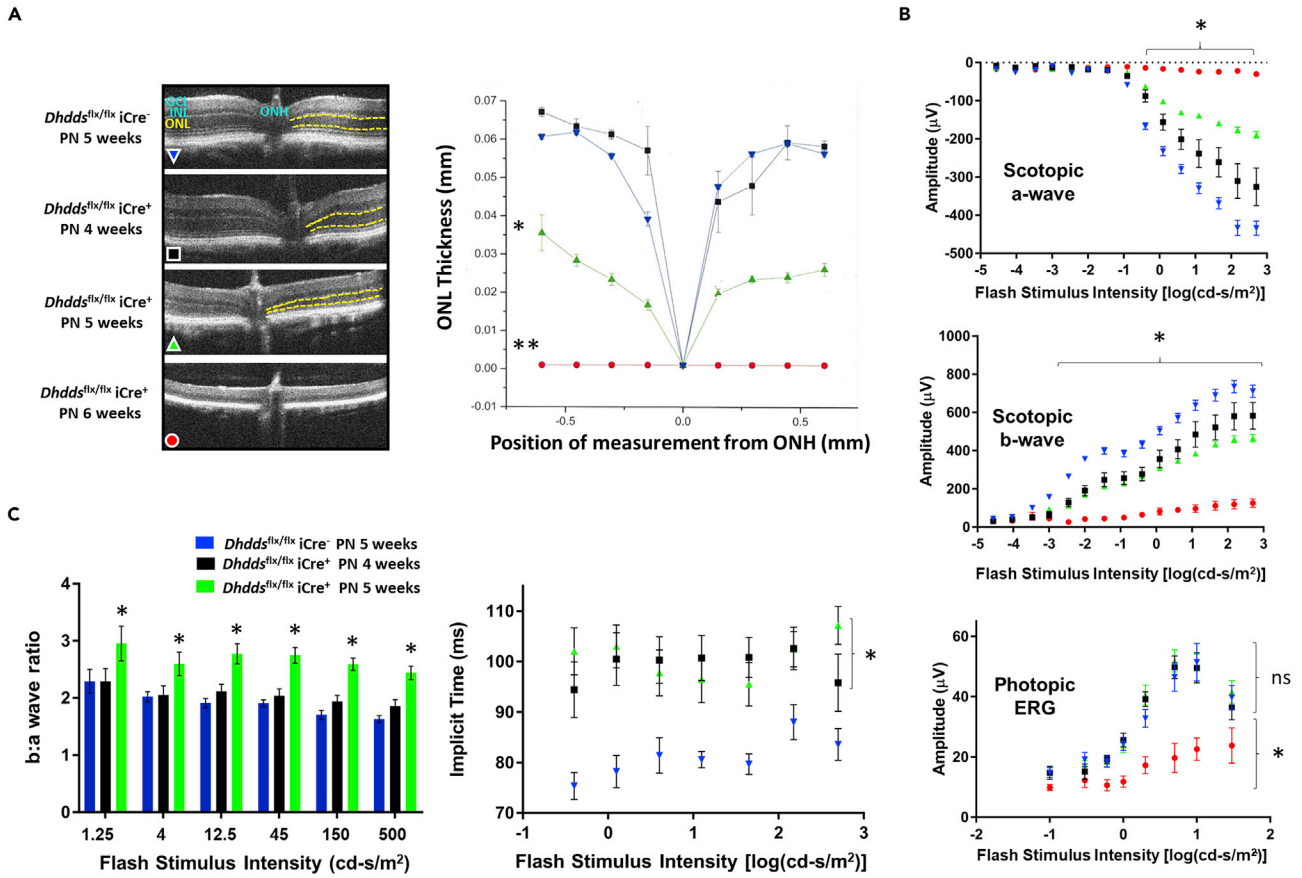

Figure 3. Retinal Thinning and Light Response Deficits in *Dhdds*$^{flx/flx}$ iCre^{+}Mice

(A, left panel) Retinal thickness in *Dhdds*$^{flx/flx}$ iCre^{+} and age-matched controls (n = 4/age group) was measured using SD-OCT. The panel provides representative SD-OCT images (including optic nerve head [ONH]) comparing *Dhdds*$^{flx/flx}$ iCre^{-} controls with *Dhdds*$^{flx/flx}$ iCre^{+} between PN 4 and 6 weeks (color code for experimental groups for all panels has been provided within the OCT panel). The ONL is demarcated by yellow dotted lines. (A, right panel) Graphical representation of the measured ONL thickness (in mm) in *Dhdds*$^{flx/flx}$ iCre^{+} mice and age-matched controls. *Dhdds*$^{flx/flx}$ iCre^{+} mice exhibit ONL thickness comparable to controls at PN 4 weeks and undergo significant thinning at PN 5 weeks (reduced by 50%) and PN 6 weeks (reduced by 80%–90%) (n = 4).

(B, *top and middle panels*) Scotopic ERG responses in *Dhdds*$^{flx/flx}$ iCre^{+} mice were markedly diminished at all time points tested, relative to age-matched *Dhdds*$^{flx/flx}$ iCre^{-} controls (flash intensity range: 10^{-4} to 500 cd-s/m^2). Both a- and b-wave amplitude maxima in response to flash stimuli were plotted as a function of flash intensity (top and middle panels, respectively). At very low flash intensities (10^{-4} cd-s/m^2), pure rod response b-wave amplitudes were significantly reduced in all age groups. Both scotopic (rod-driven) a-wave and b-wave responses of PN 6-week-old *Dhdds*$^{flx/flx}$ iCre^{+} mice were significantly decreased. (See Figure S6 for representative scotopic ERG traces at saturating flash intensity.) (B, *bottom panel*) Light-adapted, photopic (cone-driven) ERG responses of *Dhdds*$^{flx/flx}$ iCre^{+} mice were comparable to those of controls at PN 4 and 5 weeks, despite reduced photopic responses at those time points. However, *Dhdds*$^{flx/flx}$ iCre^{+} photopic ERG responses were minimal at PN 6 weeks and differences were statistically significant compared with age-matched controls.

(C, *left panel*) Scotopic b:a wave magnitude ratios were significantly increased at all flash intensities ≥1.25 cd-s/m^2 in PN 5-week-old *Dhdds*$^{flx/flx}$ iCre^{+} mice, when compared with age-matched controls. (C, *right panel*) Scotopic b-wave implicit times were significantly lengthened in both PN 4- and 5-week-old *Dhdds*$^{flx/flx}$ iCre^{+} mice, when compared with controls, for all flash intensities ≥0.4 cd-s/m^2. (n = 12 for control; n = 9 for *Dhdds*$^{flx/flx}$ iCre^{+} PN 4 weeks; n = 12 for *Dhdds*$^{flx/flx}$ iCre^{+} PN 5 weeks; n = 7 for *Dhdds*$^{flx/flx}$ iCre^{+} PN 6 weeks). *p < 0.05, **p < 0.01; Welch's (unpaired) t test.

channel, Figure 4B). GFAP decorates only astrocytes and the Müller glial "endfeet" (i.e., the so-called inner limiting membrane) in a representative control retina (*green* channel, Figure 4A). Anti-opsin immunohistochemistry (*red* channel, Figure 4B) revealed dramatic shortening of ROS in *Dhdds*$^{flx/flx}$ iCre^{+} mice at PN 5 weeks, when compared with controls (*red* channel, Figure 4A), fully consistent with the ERG results (see earlier discussion).

Defective trafficking ("mislocalization") of opsin has been observed in animal models using either tunicamycin-induced or genetic inhibition of global proteome glycosylation (Murray et al., 2015; Fliesler and

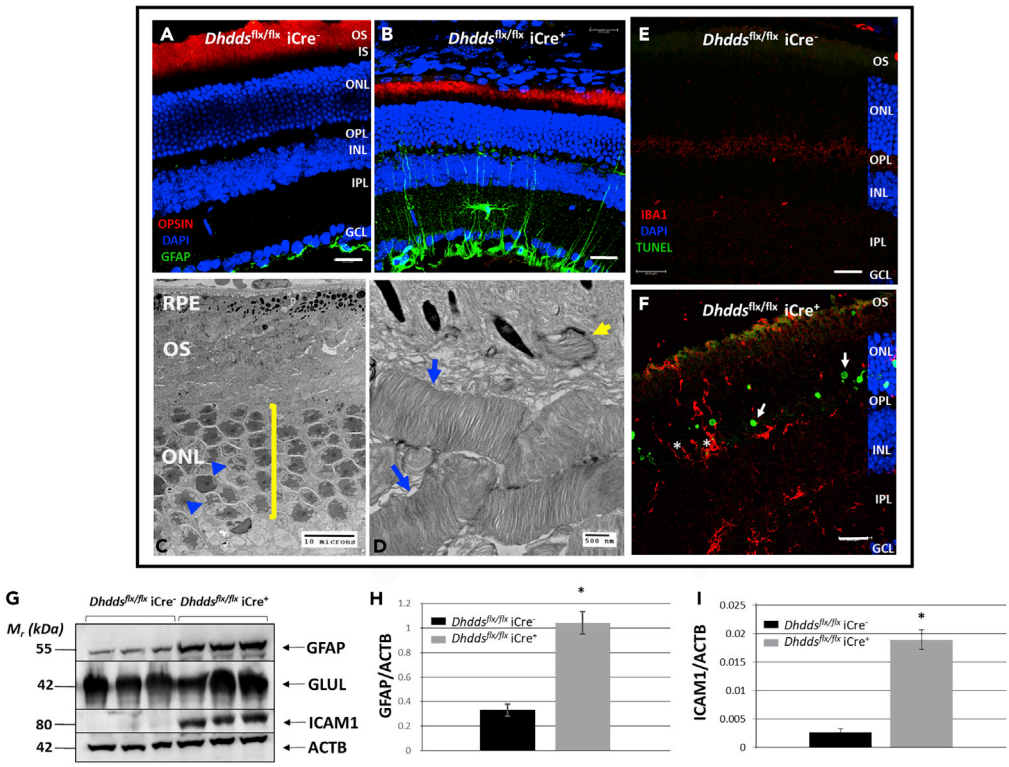

Figure 4. Morphological and Degenerative Features of the Dhdds$^{flx/flx}$ iCre^{+} Retina

(A and B) Confocal micrographs of (A) *Dhdds*$^{flx/flx}$ iCre^{-} and (B) *Dhdds*$^{flx/flx}$ iCre^{+} mouse retinas at PN 5 weeks of age. Note the shortening of rod outer segments (detected using anti-opsin; *red* channel) in *Dhdds*$^{flx/flx}$ iCre^{+} retina (B) and the accompanying gliosis (detected using anti-GFAP; *green* channel). GFAP labeling was limited to Müller glial endfeet and astrocytes (comprising the internal limiting membrane at the vitreoretinal interface) in controls (A). *Dhdds*$^{flx/flx}$ iCre^{+} mice did not exhibit anti-opsin immunostaining in either the inner segments (IS) or the photoreceptor perinuclear space, suggesting unhindered opsin trafficking (scale bars, 20 μm).

(C and D) Electron micrographs of *Dhdds*$^{flx/flx}$ iCre^{+} outer retina at PN 5 weeks, indicating grossly shortened and poorly aligned, but otherwise ultrastructurally normal, outer segments (OS) (*blue arrows*, D) and functional RPE phagocytosis (*yellow arrow*, D). Note pyknotic nuclei (*blue arrowheads*, C) and thinning of ONL (6 nuclei in a row, *yellow bracket*, C). Scale bars: 10 μm in (C) and 500 nm in (D).

(E) *Dhdds*$^{flx/flx}$ iCre^{-} retina did not exhibit TUNEL labeling. Iba-1 immunoreactivity of microglial cell bodies and arbors was limited to few cell bodies in PN 4- to 5-week-old *Dhdds*$^{flx/flx}$ iCre^{-} retina (see Figure S8D) (scale bar: 20 μm).

(F) Retinal dystrophy in *Dhdds*$^{flx/flx}$ iCre^{+} mice was characterized by photoreceptor-specific autonomous cell death, as evidenced by TUNEL labeling (*white arrows*, 488-nm channel). Autonomous cell death in *Dhdds*$^{flx/flx}$ iCre^{+} mice was accompanied by infiltration of Iba-1-positive microglia (*red* channel) into the ONL and subretinal space (*white arrows*. Furthermore, we observed microglial phagocytosis of TUNEL-negative photoreceptors ("phagoptosis") leading to non-autonomous cell death (denoted by *asterisks*) (scale bar: 20 μm).

(G) Western blot analysis and semi-quantitative densitometry indicates significant up-regulation of GFAP (marker of gliosis) and ICAM-1 (facilitates trans-endothelial migration of leukocytes and breakdown of the blood-retinal barrier). GLUL and ACTB served as loading controls for Müller glia and total protein, respectively. (H) Quantification of GFAP levels in *Dhdds*$^{flx/flx}$ iCre^{-} (*black*) vs. *Dhdds*$^{flx/flx}$ iCre^{+} (*gray*) mouse retinas on Western blots (see G), normalized to ACTB. (I) Quantification of ICAM1 levels in *Dhdds*$^{flx/flx}$ iCre^{-} (*black*) vs. *Dhdds*$^{flx/flx}$ iCre^{+} (*gray*) mouse retinas on Western blots (see G), normalized to ACTB. *p < 0.05, **p < 0.01; Welch's (unpaired) t test.

Basinger, 1985; Fliesler et al., 1984a, 1985). However, in the *Dhdds*$^{flx/flx}$ iCre^{+} retina at an intermediate degenerative stage (PN 5 weeks), we did not observe such defects, e.g., inner segment/cytoplasmic accumulation of opsin, plasma membrane localization along the inner segment, and even to the synaptic terminal. Despite shortening of ROS, opsin trafficking was comparable to that of age-matched control (Figures 4A and 4B). We utilized an established murine model of autosomal dominate RP (adRP)—the *Nog*$^{Rho-/-}$ mouse, harboring mutations of the two N-terminal asparagine residues, N2 and N15—to demonstrate the trafficking fate of opsin in an animal model of true opsin hypoglycosylation. IHC revealed

opsin accumulation in the inner segment, perinuclear space, as well as synapses of *Nog*$^{Rho-/-}$ retinas (*white arrows*, Figure S7). Furthermore, low- and high-magnification electron micrographs (Figures 4C and 4D, respectively) of *Dhdds*$^{flx/flx}$ iCre^{+} retinas also suggested thinning of the ONL (*yellow bracket*, Figure 4C) and disorganized ROS (*blue arrows*, Figure 4D), but with normal lamellar disk membrane ultrastructure (Figure 4D). Surprisingly, despite the rod-specific and essentially quantitative ablation of *Dhdds*, these observations are not comparable with pathological features in models of opsin glycosylation defects.

We evaluated whether the rapid thinning of the outer retina was due exclusively to rod cell death, owing to the rod-specific deletion of *Dhdds*. For this purpose, formaldehyde-fixed, paraffin-embedded sections of eyes from *Dhdds*$^{flx/flx}$ iCre^{+} and control mice (at PN 5 weeks, a time point at which the retina is in an intermediate stage of degeneration) were subjected to TUNEL analysis. Confocal fluorescence microscopy revealed TUNEL labeling (*green* channel) exclusively in the ONL of the *Dhdds*$^{flx/flx}$ iCre^{+} retina (Figure 4F; *white arrows*, Figures S8A–S8C); the labeling pattern was consistent with that expected for rod (not cone) PRs. Control retinas did not exhibit TUNEL-positive labeling, as expected (Figure 4E). These data are consistent with the ERG data described earlier in the discussion, suggesting a role for autonomous rod PR cell death in the observed ONL thinning.

We further observed that PR cell death was accompanied by phagocytosis of *live*, TUNEL-*negative* neurons by activated microglia, as has been reported for other models of retinal degeneration (Zhao et al., 2015). IHC analysis using antibodies to Iba-1 (a faithful marker of microglia) in *Dhdds*$^{flx/flx}$ iCre^{+} mice revealed infiltration of activated microglia into the ONL (*asterisk*, Figure 4H) as well as the subretinal space (i.e., the zone normally occupied by PR outer segments) (*arrows*, Figures 4H and S9A–S9C). By contrast, age-matched control retinas showed horizontally ramified microglia in the inner retinal layers only, as expected (Figures 4G and S8D). Representative high-magnification confocal microscopic images of activated microglia with phagocytic cups engulfing PR soma were observed (*red* arrows, Figure S8F). Activated microglia/macrophages in the subretinal space were quantified (utilizing hematoxylin and eosin [H&E] staining) as the number of nuclei in the typically acellular subretinal space (n = 3 sections of 10 μm thickness per animal, n = 8/group) (*black arrows*, Figures S8A and S8B). *Dhdds*$^{flx/flx}$ iCre^{+} mice exhibited a 4-fold increase in the number of nuclei in the subretinal space, when compared with the same region of the retina in age-matched controls (nuclei in the subretinal space were observed only in peripheral retina of WT mice). This was further observed as DAPI-positive, Iba-1-positive cells (interpreted as microglia/macrophages) in the subretinal space (*white arrowheads*, Figures 4F, S8E, S9A, and S9B)

Because Iba-1 immunoreactivity is indicative of an endogenous immune response, we adopted an unbiased (''shotgun'') cytokine screening approach to reveal other molecular players in the observed retinal degeneration. Surprisingly, the only two prominent targets with significant change (>2-fold increase) that emerged in *Dhdds*$^{flx/flx}$ iCre^{+} retinas, when compared with age-matched controls, were ICAM-1 and CXCL-10. Cytokine array data along with quantification are provided in Figure S10. Up-regulation of ICAM-1 and GFAP in *Dhdds*$^{flx/flx}$ iCre^{+} retinas (n = 3/group) was further validated by western blot analysis and semi-quantitative densitometry. Whole retinal ICAM-1 and GFAP levels were approximately 8- and 4-fold higher (n = 3/group), respectively, in *Dhdds*$^{flx/flx}$ iCre^{+} retinas compared with age-matched controls (Figures 4G–4I). Glutamine synthetase (GLUL) and β-actin (ACTB) served as loading controls for Müller glia and total retinal protein, respectively (Figure 4G).

Protein N-glycosylation Is Active in the Dhdds$^{flx/flx}$ iCre^{+} Retina

We investigated the glycosylation status of proteins in PN 5-week-old *Dhdds*$^{flx/flx}$ iCre^{+} retinas compared with retinas from age-matched *Dhdds*$^{flx/flx}$ iCre^{-} mice (which served as controls, instead of WT mice). This was achieved by adopting a dual-lectin staining strategy that exhibits differential binding of lectins to rod versus cone PRs: Concanavalin-A (Con-A, a lectin with specific affinity for non-reducing α-D-mannosyl and α-D-glucosyl residues and which binds to the interphotoreceptor rod matrix sheath) and peanut agglutinin (PNA, a lectin that preferentially binds to galactosyl-β(1,3)-N-acetylgalactosamine, a constituent of the interphotoreceptor cone matrix sheath) (Varner et al., 1987; Hageman and Johnson, 1986). If *Dhdds* ablation inhibited *N*-glycosylation as hypothesized, we expected to observe a lack of Con-A binding to rod PRs. Surprisingly, Con-A labeling of the rod-rich outer retinal layer of *Dhdds*$^{flx/flx}$ iCre^{+} mice at PN 5 weeks was robust (including ROS, ONL, and outer plexiform layer [OPL]), comparable to age-matched controls (*green* channel, Figures 5A and 5B). PNA staining (*far-red* channel, pseudocolored *magenta*) suggested that cone PR density and distribution in rod-*Dhdds*-null mice was not altered at PN 5 weeks (Figures 5A–5D). PNGase-

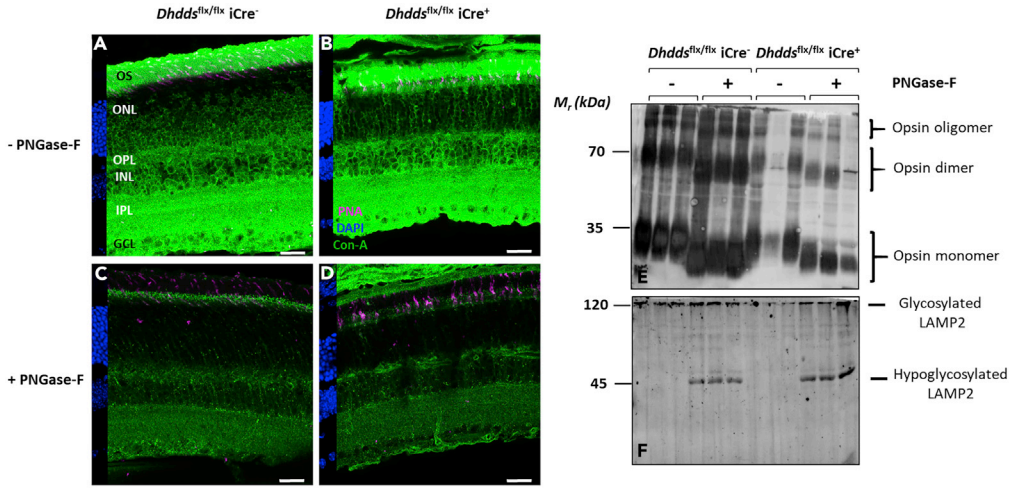

Figure 5. Protein *N*-Glycosylation is Functional in the *Dhdds*$^{flx/flx}$ iCre^{+} Retina

(A–F) The glycosylation status of *Dhdds*$^{flx/flx}$ iCre^{+} retinas (PN 5 weeks) was evaluated and compared with that of controls using a dual-lectin cytochemical staining strategy (Concanavalin-A [Con-A] in *green* channel, and cone PR-specific peanut agglutinin [PNA] in *far-red* [pseudocolored *magenta*] channel). Confocal fluorescence micrographs demonstrate robust Con-A labeling in *Dhdds*$^{flx/flx}$ iCre^{+} retina (B) comparable to that in controls (A), suggesting normal protein *N*-glycosylation in *Dhdds*$^{flx/flx}$ iCre^{+} mouse retinas. This was validated by testing the PNGase-F sensitivity of Con-A binding. Both control and *Dhdds*$^{flx/flx}$ iCre^{+} retinas (C and D, respectively) were sensitive to PNGase-F activity and exhibited markedly reduced Con-A binding. Furthermore, cone density and distribution (as indicated by PNA binding) was comparable in both control and *Dhdds*$^{flx/flx}$ iCre^{+} retinas. PNA labeling was unaffected by PNGase-F treatment, because PNGase-F does not cleave the cognate disaccharide Gal-β(1,3)-GalNAc to which PNA binds. Scale bars: 20 μm in (A–D). Retinal protein extracts from *Dhdds*$^{flx/flx}$ iCre^{+} and control mice (n = 3/group, at PN 5 weeks) were subjected to PNGase-F treatment, and western blot analysis was performed, probing the blot with antibodies to opsin (RHO) and LAMP2 (E and F, respectively). Untreated protein extracts served as negative controls for PNGase-F treatment. Opsin and LAMP2 proteins from *Dhdds*$^{flx/flx}$ iCre^{+} retinas exhibited PNGase-F sensitivity, and a subsequent M_r mobility shift (from ~37 to ~35 kDa, and from ~120 to ~40 kDa, respectively) as a consequence of cleaving their *N*-linked glycans, relative to the lanes containing untreated retinal extracts. This same behavior was observed when retinal extracts from control mice were subjected to PNGase-F treatment. Hence, RHO and LAMP2 were *N*-glycosylated in *Dhdds*$^{flx/flx}$ iCre^{+} mice. Note the decreased levels of opsin in lanes corresponding to *Dhdds*$^{flx/flx}$ iCre^{+}, when compared with controls.

F-treated sections subsequently subjected to dual lectin staining were utilized as true "negative" controls (Figures 5C and 5D), as PNGase-F treatment should remove all N-linked glycans and, hence, abolish Con-A binding. Similar to Con-A labeling, wheat germ agglutinin (which detects N-acetyl-D-glucosamine residues) also exhibited robust binding to *Dhdds*$^{flx/flx}$ iCre^{+} retinas, comparable to that of controls (Figure S11).

We further verified protein *N*-glycosylation in *Dhdds*$^{flx/flx}$ iCre^{+} retinas by examining PNGase-F sensitivity of opsin (the most abundant rod PR-specific glycoprotein) and LAMP2 (lysosome-associated membrane glycoprotein). Opsin and LAMP2 western blot analysis of PNGase F-treated versus untreated retinal protein extracts from *Dhdds*$^{flx/flx}$ iCre^{+} and control mice at PN 5 weeks was consistent with the lectin cytochemical staining results described earlier in the article. Both opsin and LAMP2 from *Dhdds*$^{flx/flx}$ iCre^{+} retinas (Figures 5E and 5F) were sensitive to PNGase-F treatment, and exhibited mobility shifts relative to the untreated specimens (biological triplicates), as expected. These findings were comparable to those obtained with PNGase-F-treated versus untreated control retinas (Figures 5E and 5F).

Retinal Dolichol Levels Are Markedly Reduced in Dhdds$^{flx/flx}$ iCre^{+} Mice

Age-dependent reduction of PR number in *Dhdds*$^{flx/flx}$ iCre^{+} retinas (Figures 3A and 3B) presents a challenge in delineating the expected decrease in total dolichol content due to ablation of *Dhdds*, as opposed to the decrease in the PR population (cell mass). Therefore, we utilized retinas from PN 4-week-old *Dhdds*$^{flx/flx}$ iCre^{-} and *Dhdds*$^{flx/flx}$ iCre^{+} mice to measure whole retinal dolichol content—a time point at which no significant attrition in PR mass was observed (Figures 3A and 3B). For mass spectrometry

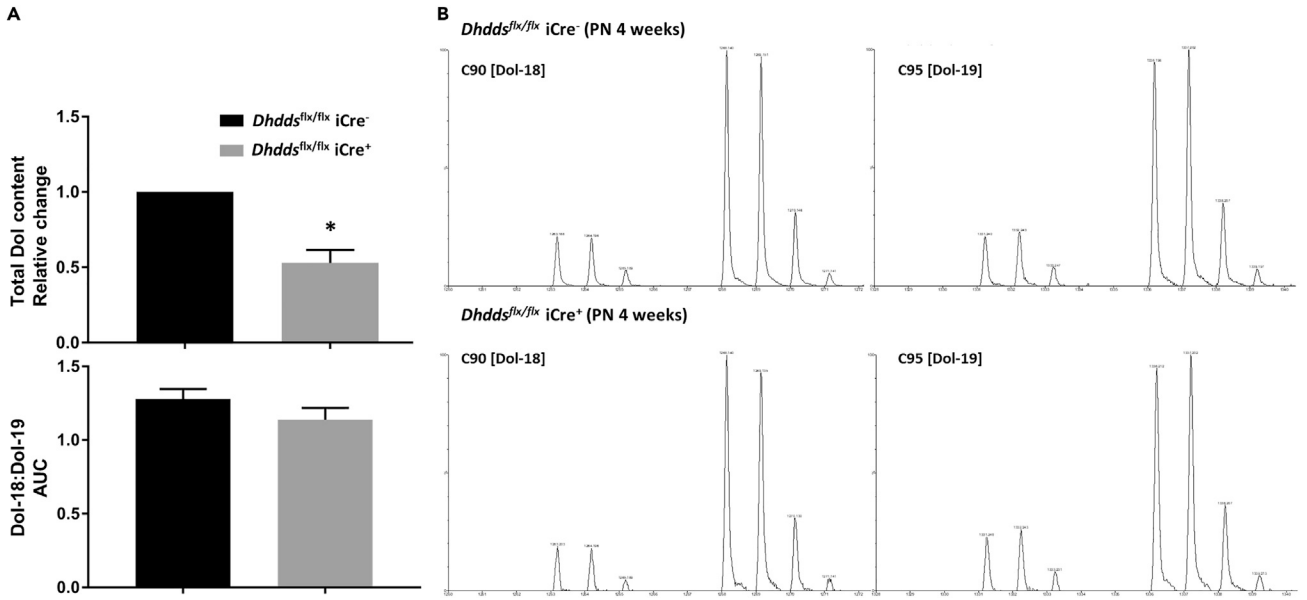

Figure 6. Dolichol Content Is Markedly Decreased in *Dhdds*$^{flx/flx}$ iCre^{+} Retinas, Relative to Age-Matched Controls

(A) LC-MS analysis of dolichols extracted from *Dhdds*$^{flx/flx}$ iCre^{+} and control retinas demonstrated ~50% decrease in the total dolichol content of *Dhdds*$^{flx/flx}$ iCre^{+} retinas (n = 4), when compared with controls (n = 3) (*upper panel*, A). However, there was no selectivity as a function of dolichol chain lengths: the Dol-18:Dol-19 ratio [C90:C95] in *Dhdds*$^{flx/flx}$ iCre^{+} retinas was comparable to that of age-matched controls (*lower panel*, A).

(B) Mass spectra of Dol-18 and Dol-19 species from *Dhdds*$^{flx/flx}$ iCre^{-} (control) and *Dhdds*$^{flx/flx}$ iCre^{+} retinas. Note that signals of ammoniated $[M + NH_4]^+$ and sodiated $[M + Na]^+$ forms of respective Dol isotopologues are clearly visible. Each sample analyzed was prepared by pooling five retinas from the respective genotype group. *$p < 0.05$; Welch's (unpaired) t test.

quantification of dolichol, five retinas were pooled per sample to obtain sufficient tissue mass (n = 3 for *Dhdds*$^{flx/flx}$ iCre^{-} mice, n = 4 for *Dhdds*$^{flx/flx}$ iCre^{+} mice). Liquid chromatography-mass spectrometry (LC-MS) analysis was performed to quantify the two dominant dolichol species—C90 (Dol-18) and C95 (Dol-19) (denoting dolichol species with 18 or 19 isoprene units and containing 90 or 95 carbon atoms, respectively); the sum of C90 plus C95 species was taken to represent the total retinal dolichol content. As shown in Figure 6 (*top panel*, Figure 6A), retinas from *Dhdds*$^{flx/flx}$ iCre^{+} mice exhibited about a 50% reduction ($p < 0.01$) in total dolichol content, relative to *Dhdds*$^{flx/flx}$ iCre^{-} (control) retinas. Despite this, the distribution of dolichol species remained unaltered: no significant difference was observed in the ratio of Dol-18 to Dol-19 (*bottom* panel, Figure 6A). Representative mass spectra of C90 and C95 dolichols from *Dhdds*$^{flx/flx}$ iCre^{+} retinas are shown in Figure 6B.

DISCUSSION

Several *in vivo* biochemical, pharmacological, and genetic studies (Fliesler et al., 1984a, 1985; Kean, 1980; Fliesler and Basinger, 1985; Murray et al., 2015) have demonstrated retinal *de novo* synthesis of dolichol and the requirement of dolichol-dependent *N*-glycosylation in maintaining the normal structure and function of the retina, particularly as regards the intracellular trafficking and incorporation of opsin, the predominant PR-specific glycoprotein, into ROS membranes. Recent whole-exome sequencing studies have revealed the RP59-causative missense mutations in the gene coding for DHDDS, which catalyzes the committed step of the mevalonate pathway directed toward dolichol synthesis (Zelinger et al., 2011; Zuchner et al., 2011). The present study is the first to employ a genetic approach, using conditional deletion of DHDDS in retinal rod PRs, to study the effects of altered PR dolichol homeostasis, as a tractable step toward understanding the pathological mechanisms underlying RP59. The following discussion provides broad insights into the challenges in modeling a complex metabolic disorder pertaining to dolichol homeostasis and compares the findings of this study (i.e., rapid structural and functional degeneration of PRs and markedly decreased dolichol content, but *without* any obvious impact on protein N-glycosylation), using a murine model, with the human RP59 disease.

Important Considerations in Generation and Verification of Rod PR-Specific Dhdds Knockout Mice

Multiple rod PR-specific, Cre recombinase-expressing mouse lines (driven by rod PR-specific Nrl,/LMOP/RHO promoters) may be utilized for the targeted excision of the loxP-modified gene of interest selectively in rod cells (Brightman et al., 2016; Le et al., 2006; Li et al., 2005). We set out to compare the spatiotemporal expression/activity of Cre recombinase in two Cre lines (LMOP-Cre and Rho-iCre75), utilizing the ZsGreen reporter strategy (Figures 2D,S3, and S5). The Rho-iCre75 mouse line exhibited Cre recombinase activity in almost all terminally differentiated rod PRs (Figure S5 and 2D), in good agreement with the original report describing the Rho-iCre75 mouse line (Li et al., 2005), whereas the LMOP-Cre line exhibited mosaic Cre-recombinase activity (ZsGreen reporter expression in ~30%–40% of rod PRs only at PN 90 days) (Figure S12). Therefore, we utilized the Rho-iCre75 line to generate the *Dhdds*$^{flx/flx}$ iCre^{+} model, which successfully induced *Dhdds* deletion in terminally differentiated rod PRs. Importantly, Cre expression in the Rho-iCre75 line commences at around PN day 7; at that stage of retinal development, rod cell fate has been determined, but initiation of ROS assembly has just barely commenced and full maturation of rods has yet to be achieved.

Tail snip genotyping does not provide direct evidence for exon excision in the target tissue/cell type. Owing to the lack of availability of reliable antibodies against murine DHDDS, it is challenging to directly verify DHDDS protein levels, or cell type-specific knockout of the target. Therefore, we verified the establishment of this model by multiple approaches: (1) indirect tail snip genotype analysis (Figure S4), (2) direct retinal genotyping (testing whole tissue genomic DNA extract for *Dhdds* excision, Figure 2C), (3) the ZsGreen reporter mouse approach to detect Cre-recombinase activity (Figure 2D), and (4) ISH (Figures 2E and 2F) to obtain histology-level verification of cell type-specific *Dhdds* ablation. PCR assay involving whole retinal genetic material utilized a short extension period to only select for the 584-bp intronic PCR product (upon exon excision). One would predict that using a long extension period would amplify the long, non-excised *Dhdds* allele arising from other retinal cell types and may not distinguish heterozygous from homozygous knockouts. Therefore, retinal genotyping, when preceded by preliminary tail snip analysis (to confirm *loxP* homozygosity), and the reporter mouse strategy may provide better qualitative evidence for target excision. ISH using an RNA-based technology (BaseScope; ACD Bio) to probe control and *Dhdds*$^{flx/flx}$ iCre^{+} retinas (Figures 2E and 2F) provided important morphological and physiological context regarding *Dhdds* expression in the retina, as well as direct verification of successful *Dhdds* excision in a cell type-specific manner. Importantly, ISH labeling of the adjacent INL provides an on-section internal positive control for validating *Dhdds* mRNA detection by the BaseScope ZZ probes.

DHDDS belongs to the superfamily of CPT enzymes involved in the synthesis of long-chain polyisoprenoid products upon *cis*-condensation of FPP and IPP (yielding $\geq C_{55}$ long-chain products). Structural elucidation of *E. coli* undecaprenyl pyrophosphate synthase (UPPS) has revealed critical amino acids involved in hydrogen bonding and hydropathic interactions with FPP and IPP (Guo et al., 2005). Multiple sequence analysis using CLUSTALW2 algorithm suggests that these critical amino acids are well conserved in murine DHDDS CPT and other mammalian CPT enzymes (compare Figures S1 and S2) (Larkin et al., 2007). Targeted ablation of coding exon 3 of *Dhdds* is predicted to render the enzyme fully inactive due to the loss of the amino acids required for hydropathic interaction with FPP and hydrogen bonding with the phosphate groups of IPP (Figures S1 and S2). Furthermore, compensatory mechanisms for dolichol synthesis can be ruled out due to the absence of DHDDS homologs.

Whole-exome sequencing of patients with RP59 revealed point mutations in the DHDDS gene, the predominant mutation being K42E. The K42E mutation renders the human DHDDS gene product *hypoactive*, unlike the mouse rod-specific *Dhdds* exon 3 knockout (with expected total loss of function of DHDDS activity) (Figure S2). Another reported pathogenic DHDDS mutation is W64X (phenylalanine to STOP codon), which resulted in early postnatal lethality (Sabry et al., 2016). This clinically "severe" mutation generates a fully dysfunctional gene product comparable to the loss of the DHDDS catalytic activity in the *Dhdds*$^{flx/flx}$ iCre^{+} mouse model. The *Dhdds*$^{flx/flx}$ iCre^{+} mouse model differs from the human RP59 disease in at least two respects: (1) the RP59-causing DHDDS mutations (see Figure S3) globally affect all tissues and cell types, including the retina, whereas our mouse knockout model employs targeted *Dhdds* ablation only in rod PRs and (2) the predominant RP59 point mutation, K42E, is only hypomorphic, whereas our knockout model is a total loss-of-function insult, although cell type specific. Despite these differences, the findings in this study suggest that conditional deletion of *Dhdds* in rod PRs is sufficient to elicit a profound and rapid retinal degeneration. Furthermore, the *Dhdds*$^{flx/flx}$ iCre^{+} mouse line serves as a reliable biochemical model (owing to the presumed complete loss of DHDDS activity) to investigate the rod PR requirement for the dolichol pathway (Figure S2).

Structural, Functional, and Pathological Consequences of Rod Photoreceptor-Specific Dhdds Deletion

The current study was aimed at investigating the PR-specific disease mechanism(s) of RP59. *In vivo* retinal imaging (SD-OCT analysis, Figure 3A) suggested that ONL thickness in *Dhdds*$^{fl\times/fl\times}$ iCre^{+} mice was comparable to that of age-matched controls at PN 4 weeks. Surprisingly, the unaltered structural integrity at PN 4 weeks in *Dhdds*$^{fl\times/fl\times}$ iCre^{+} retinas did not correspond to full *functional* integrity (see Figures 3B, and S6): scotopic ERG responses (a- and b-waves) at all flash intensities (10^{-4} to 500 cd-s/m^2) were significantly lower compared with those of age-matched (PN 4 weeks) controls. *Dhdds*$^{fl\times/fl\times}$ iCre^{+} retinas exhibited both profound structural and functional deficits at PN 5 and 6 weeks. ONL thickness was significantly reduced at PN 5 weeks (by ~50% [$p < 0.05$], compared with age-matched WT C57BL/6J controls, Figure 3B). Low-magnification images of H&E-stained sections of eyes from PN 5-week-old *Dhdds*$^{fl\times/fl\times}$ iCre^{+} mice showed PR thinning (Figures S13B and S13D) compared with age-matched controls (Figures S13A and S13C). The rapid PR loss observed in *Dhdds*$^{fl\times/fl\times}$ iCre^{+} mice can be attributed to the following two degenerative processes: (1) autonomous rod PR-specific cell death, as observed by TUNEL labeling, and (2) phagocytosis of live PRs by activated, Iba-1-positive microglia (Figures 4F, S8E, S8F, and S9), leading to *non*-autonomous loss of PRs. The exact details of rod PR-autonomous defective cell processes leading to cell death upon *Dhdds* deletion remain to be elucidated. The *Dhdds*$^{fl\times/fl\times}$ iCre^{+} mice also exhibited activated microglia in the subretinal space, i.e., between the outer neural retina and the underlying retinal pigment epithelium (Figures 4F, S8E, S8F, and S9), which is normally "virtual" space filled with PR outer segments and associate extracellular matrix constituents. By contrast, the microglial population in retinas of young, age-matched control mice was notably sparse, and restricted to just the inner retinal layers (nner plexiform layer [IPL], ganglion cell layer [GCL]), as judged by Iba-1 immunostaining (Figures 4E and S8D). Although previous investigators have made similar observations regarding the distribution of microglia in the normal C57BL/6 mouse retina (Xu et al., 2007; Kaneko et al., 2008; Chen and Xu, 2015), often the Iba-1-positive cells were more numerous than what we observed in the present study. The reasons for these differences are not fully apparent, but could be due to age-dependent population differences (e.g., prior studies tended to use older mice than those employed here), or possibly to differences in the type of embedment media used (i.e., optimal cutting temperature embedment medium [O.C.T.] frozen sections versus paraffin sections) (Atiskova et al., 2019; Noailles et al., 2019). Proteomic and/or transcriptomic approaches offer potentially fruitful avenues to investigate the downstream cellular and molecular processes that are altered upon *Dhdds*-dependent inhibition of dolichol synthesis. Pharmacological inhibition of microglial activity in the retina also may provide a therapeutic avenue for preventing the rapid retinal degeneration observed in the *Dhdds*$^{fl\times/fl\times}$ iCre^{+} mouse model. Our cytokine array analysis (and correlative western blot analysis) revealed >8-fold up-regulation of ICAM-1 levels in *Dhdds*$^{fl\times/fl\times}$ iCre^{+} retinas compared with age-matched controls; such has been implicated in leukocyte adhesion, as well as breakdown in the blood-retinal barrier (Williams and Luscinskas, 2011; Devine et al., 1996; Mesri et al., 1994). The presumed involvement of ICAM-1 in microglial recruitment and in the observed retinal degeneration in this animal model also remains to be investigated further. Another key degenerative feature of the *Dhdds*$^{fl\times/fl\times}$ iCre^{+} retina is gliosis, as evidenced by significant up-regulation of GFAP relative to that of the Müller glial marker glutamine synthetase (Figures 4B and 4G–4I).

The SD-OCT results (i.e., ONL thinning) demonstrated rapid retinal degeneration in *Dhdds*$^{fl\times/fl\times}$ iCre^{+} mice; however, whereas most of that loss reasonably could be attributed to rod cell degeneration and demise (given that rods account for ~97% of the PRs in the mouse retina; Carter-Dawson and Lavail, 1979), the involvement of cone degeneration and demise cannot be discounted. Cone function was directly assessed utilizing photopic ERG analysis at all tested time points (PN 4, 5, and 6 weeks) (Figure 3B, bottom panel). Electrophysiological responses of cone PRs were unaltered and robust until massive rod dropout was observed at PN 6 weeks (Figure 3B, bottom panel), suggesting a rapid rod-cone dystrophy. The rod-cone dystrophy observed in this animal model, although consistent with the rod-cone dystrophy observed in patients with RP59 (Kimchi et al., 2018), should be interpreted with caution. The rod-cone dystrophy observed in the *Dhdds*$^{fl\times/fl\times}$ iCre^{+} mouse model is "by design," i.e., rod PR primary cell death is attributable to the rod-targeted excision of *Dhdds*, whereas cone PRs exhibit secondary dysfunction (i.e., a "bystander effect"; Ripps, 2002; Cusato et al., 2006; Ma et al., 2018), which is independent of *Dhdds* activity. Cone-specific PNA staining, as expected, did not reflect any significant cone PR dropout even at PN 5 weeks (Figures 5C and 5D). The density and distribution of PNA-positive structures in *Dhdds*$^{fl\times/fl\times}$ iCre^{+} mouse retinas appeared qualitatively comparable to that of age-matched controls, in agreement with the photopic ERG responses observed at PN 5 weeks (Figure 4C). PNA binds to *O*-linked glycans (specifically, the disaccharide Gal-β(1–3)-GalNAc), and therefore its binding to cone PRs is unaltered by PNGase-F treatment. We further documented cone arrestin distribution in PN 5-week-old *Dhdds*$^{fl\times/fl\times}$ iCre^{+} retinas, compared with age-

matched controls. We observed cone arrestin-positive structures both in the inner/outer segment region and in the OPL (PR synapses) (Figures S13C and S13D).

Furthermore, we observed age-dependent increase in the scotopic b:a wave ratio (Figure 3C, left panel), in accordance with severe reductions in scotopic a-wave amplitudes, in relation to the reduction in b-wave amplitude. A similar increase in b:a wave ratio has been described in patients with PMM2-CDG (Thompson et al., 2012). However, we observe a significant decrease in both scotopic b-wave and a-wave amplitudes in the *Dhdds*$^{flx/flx}$ iCre^{+} mice. Given that the *Dhdds* excision occurs exclusively in rod PRs, we interpret the increase in b:a wave ratio to be due to a significant and specific decrease in the a-wave component of the ERG. In addition, implicit times for *Dhdds*$^{flx/flx}$ iCre^{+} mice were significantly longer compared with those of controls (Figure 3C, right panel). This finding along with the ERG amplitude analysis at all flash intensities clearly suggest less robust and more sluggish scotopic response in *Dhdds*$^{flx/flx}$ iCre^{+} mice compared with age-matched controls. The increased b:a wave ratio in the conditional *Dhdds*$^{flx/flx}$ iCre^{+} mouse model may not be directly suggestive of similar trends in patients carrying *systemic* DHDDS point mutations; however, a:b wave ratios have not been characterized, to date, in the DHDDS-CDG patient population.

In summary, the key features of this novel *Dhdds*$^{flx/flx}$ iCre^{+} model include progressive ROS shortening, gliosis, PR cell death, and microglial activation, microglial migration to ONL and subretinal space, and phagoptosis of entire PR cells, leading to rapid rod-cone dystrophy by PN 5–6 weeks (Figures 2, 3, and 4). The findings in this model (characterized by presumed total loss of DHDDS CPT activity) may be important in ultimately understanding the underlying mechanisms involved in RP59 (caused by homozygous point mutations with mildly hindered CPT activity). Parallel efforts to this work in our laboratories currently involve generation of DHDDS dual point mutant knock-in mice harboring both K42E and T206A mutations, to create a potentially more representative model of RP59 (unpublished studies). Surprisingly, the K42E homozygous knock-in model (even up to PN 1 year of age) does not replicate the structural or functional deficit features observed either in patients with RP59 or in the *Dhdds*$^{flx/flx}$ iCre^{+} model reported here, with the exception of marked gliosis (Ramachandra Rao et al., 2020).

Biochemical Features of the Degenerating Dhdds$^{flx/flx}$ iCre^{+} Retina

We originally predicted that rod-specific *Dhdds* ablation would cause defective protein *N*-glycosylation in rods because of the biochemical requirement of protein glycosylation for Dol-P (see Figure 1) (Denecke and Kranz, 2009; Buczkowska et al., 2015; Kean, 1977, 1980, 1999; Behrens and Leloir, 1970). We first verified excision of *Dhdds* exon 3 in terminally differentiated rod PRs (Figures S5 and Figure 2) and utilized this model to analyze dolichol content and *N*-glycosylation status. However, contrary to our initial expectations, the observed rapid PR degeneration was *not* accompanied by a glycosylation defect (Figures 5 and S11). *In vitro* and *in vivo* studies involving deletion of genes encoding enzymes involved in dolichol synthesis have utilized different model systems, different genes of interest, various gene editing techniques, and different time points during cell growth/tissue differentiation. A study utilizing global ablation of *Dhdds* at the one-cell embryo stage in zebrafish, which has a cone-rich retina (unlike mouse), indicated defective protein glycosylation in the PRs, as evidenced by lack of cone PR-specific PNA staining (Zuchner et al., 2011). Mouse embryonic/conditional ablation of *NUS1*, the gene encoding NgBR, the dimeric partner of the gene product of *Dhdds*, causes embryonic lethality before E6.5, as well as loss of *N*-glycosylation (Park et al., 2014, 2016). However, curiously, biological samples (blood, urine, and fibroblasts) from patients with RP59 have been reported to exhibit a shift toward shorter dolichol chain length (increased Dol-18:Dol-19 mole ratios), without any appreciable hypoglycosylation defects (Wen et al., 2013; Lam et al., 2014). Furthermore, *DHDDS* knockdown experiments in fully confluent cell culture models did not lead to an observable glycosylation defect (Sabry et al., 2016). One possible explanation for the divergent observations across various models may involve elevated dolichol synthesis during tissue development and the unusual biological stability (long half-life) of dolichol, particularly in neural tissue. The rate of dolichol synthesis and accumulation is highest during cell growth and tissue development (Sakakihara and Volpe, 1984; Wong and Lennarz, 1982; Carson and Lennarz, 1981; Volpe et al., 1987; Adair and Cafmeyer, 1987; Doyle and Kandutsch, 1988; Larsson and Wejde, 1992). Furthermore, dolichols are biologically very stable lipids with long half-lives, and the only known forms of dolichols are the free alcohol, phosphorylated derivatives, and esters of carboxylic acids (Chojnacki and Dallner, 1988; Parentini et al., 2005). Oxidative catabolism of dolichol, although postulated, has not yet been fully documented *in vivo* (Swiezewska and Danikiewicz, 2005). It should be noted that the control and *Dhdds*$^{flx/flx}$ iCre^{+} mice utilized in this study were on a C57BL/6J background, and this study did not directly test the potential effects of other modifier mutations on the severity of the phenotype. However, we posit that the *Dhdds* K42E point knock-in mouse model may provide a better avenue to investigate the effects of genetic

background on the RP59 phenotype (Westphal et al., 2002; Slijkerman et al., 2015; Ramachandra Rao et al., 2020). LC-MS analysis of whole retinal dolichol content suggests ~50% reduction upon RhoiCre-mediated deletion of *Dhdds* in rod PRs (see Figures 2 and 6). Retinal dolichol content in our *Dhdds*$^{flx/flx}$ iCre^{+} model was significantly reduced, whereas the Dol-18/Dol-19 ratio was unaltered, unlike observations as mentioned earlier regarding tissues and fluids obtained from patients with RP59 (Wen et al., 2013) (see Figure 6). Reduction in whole retinal dolichol levels can be reasonably attributed to PR-specific loss of *Dhdds*. However, this finding may not account for any residual dolichol in PRs that may have been synthesized before Rho-iCre-mediated deletion of *Dhdds* had taken place in rod PRs (Figures 2 and S5). Future investigations into the role of mammalian DHDDS and its heterodimeric partner, NgBR, during PR genesis and retinal development may more fully explain the "hypoglycosylation-free" phenotype observed in the *Dhdds*$^{flx/flx}$ iCre^{+} mouse model described in this study (see Figures 5 and S10), as well as provide a deeper understanding of dolichol synthesis and homeostasis in retinal PRs. In addition, studying the effects of PR-specific *Dhdds* deletion on other important glycan modifications of proteins, such as *O*-mannosylation, may provide additional clues regarding the underlying mechanism driving RP59 pathology.

Inhibition of *N*-linked glycosylation perturbs vectorial trafficking of opsin and other ROS-destined proteins in PR cells and consequently compromises the inability to form PR outer segments (Fliesler et al., 1984a, 1985; Fliesler and Basinger, 1985; Ulshafer et al., 1986; Defoe et al., 1986; St Jules et al., 1990). However, surprisingly, although we observed shortening of ROS, we did not observe mislocalization of opsin, e.g., aberrant accumulation in the inner segment or in the perinuclear space of the ONL (see Figures 5A and 5B). In fact, we observed successful outer segment formation (see Figures 4C and 4D). Thus, our observations (see Figures 5 and 6) would argue *against* defective *N*-glycosylation upon Rho-iCre-mediated *Dhdds* excision, where Rho-iCre recombinase is expressed (starting at PN 7 days) *after* cell fate commitment to rod PR terminal differentiation (Li et al., 2005). However, the PR-specific ablation of *Dhdds* is sufficient to elicit primary degeneration of PRs, suggesting the requirement of continued endogenous dolichol synthesis in terminally differentiated rod PRs.

Limitations of the Study

RP59 is an autosomal recessive, non-syndromic form of RP, caused by mutations in DHDDS (Zelinger et al., 2011; Zuchner et al., 2011). Hence, although all cells require dolichol derivatives to carry out protein *N*-glycosylation, only the retina seems to be negatively impacted by such mutations in this disease. The present study was aimed at neither addressing the question of why RP59 is non-syndromic nor creating a faithful animal model that replicates the human disease phenotype. The immediate goal of the present study was to create a tractable *in vivo* model that would allow a further understanding of the requirement for dolichol homeostasis and DHDDS activity in retinal PR cells specifically. This targeted approach was taken because (1) global deletion of *Dhdds* likely would be embryonic lethal, and (2) PRs represent the predominant cell type affected in the RP59 retinal degeneration. Such targeted gene ablation in rods is best achieved by using the *Dhdds*$^{flx/flx}$ iCre^{+} model as employed here. Also, the synthesis of dolichol and its derivatives requires the activity of two enzymes— DHDDS and Nogo-B receptor (NgBR)—functioning together as a heterodimeric complex (Park et al., 2014, 2016). In this study, we have modeled the effect of PR-specific deletion of the gene that encodes only one of the two heterodimeric partners. In addition, this cell type-specific targeted gene ablation occurs only in rod PRs and is dependent on the onset of opsin gene expression (the promoter driving Cre expression), which starts at PN day 4–7 (after the onset of expression of the transcription factor *Nrl*, which determines rod cell fate). This scenario is significantly different from what occurs in human patients with RP59: first, RP59 involves DHDDS point mutations, rather than gene ablation; second, those mutations are found in every cell type throughout the retina (and the entire body), rather than being restricted just to rod cells; third, the global expression of mutant DHDDS in humans is initiated *in utero* during early embryogenesis, rather than commencing after birth.

The lack of an observable defect in protein *N*-glycosylation in the retina in the *Dhdds*$^{flx/flx}$ iCre^{+} model may be attributed to at least two factors: (1) the other heterodimeric partner, NgBR (gene: *Nus1*), required for dolichol synthesis (which, presumably, remains active in the absence of Dhdds) may be able to at least partly take over the role of Dhdds (i.e., enzyme activity is impaired, but not completely lost) and/or (2) the dolichol synthesized in PR cells (or their precursors) *before* onset of Cre-recombinase expression may persist and be sufficient to support protein *N*-glycosylation even *after Dhdds* has been ablated in the rod cells. The lack of suitable reagents or methods to directly study the distribution and turnover rates of dolichol and its derivatives at the single cell

and subcellular levels also presents a further impediment to obtaining a more complete understanding of exactly how PR-specific ablation of *Dhdds* alters this aspect of isoprenoid homeostasis in those cells.

Resource Availability

Lead Contact

Dr. Steven J. Fliesler, VA Western NY Healthcare System, Buffalo, NY 14215 U.S.A.; Email: fliesler@buffalo.edu.

Materials Availability

All novel reagents and genetically modified animals, as described herein, are available to qualified researchers per the requirements stipulated by the N.I.H., Department of Health and Human Services, USA. All associated costs must be the responsibility of the requesting investigator or institution, and are subject to review.

Data and Code Availability

Not applicable.

METHODS

All methods can be found in the accompanying Transparent Methods supplemental file.

SUPPLEMENTAL INFORMATION

Supplemental Information can be found online at https://doi.org/10.1016/j.isci.2020.101198.

ACKNOWLEDGMENTS

Supported, in part, by U.S.P.H.S. (NIH) grants 1 R01 EY029341 and a UAB Vision Science Research Center Pilot grant (S.J.P. and S.J.F.), 1UL1 TR001412 (to SUNY-University at Buffalo [S.J.F.]), P30 EY003039 (S.J.P.), EY020545 (X.M.), the National Science Centre of Poland grant no. UMO-2018/29/B/NZ3/01033 (E.S.), and by facilities and resources provided by VA Western New York Healthcare System (S.J.F.). S.J.F. is the recipient of a Research Career Scientist (RCS) Award from the Department of Veterans Affairs, BLR&D Service. S.R.R. was the recipient of two Fight for Sight Summer Student Fellowships (2013 and 2016), a Knights Templar Eye Foundation Career-Starter grant award, and a Fight For Sight Postdoctoral Fellowship. We gratefully acknowledge the technical assistance of Rebecca Benz, Cheryl Dann, and Kristie Kilby in the course of this study. We thank Drs. Muna Naash and Muayyad-Al-Ubaidi (University of Houston, Houston, TX, USA) for the generous gift of eyes from the NOG$^{Rho-/-}$ genetic murine RP model, Aimee Stablewski (Gene Targeting and Transgenic Shared Facility, Roswell Park Comprehensive Cancer Center, Buffalo, NY, USA) for the generation of *Dhdds*$^{flx/fflx}$ mice, and Dr. Jack M. Sullivan (SUNY, University at Buffalo, and VA Western NY Healthcare System, Buffalo, NY, USA) for helpful discussions and use of his ERG system during the course of this project. Finally, we thank Dr. Tirthankar Sinha (University of Houston, Houston, TX, USA) for his assistance with graphic arts. Portions of this work have been presented in preliminary form at the Annual Meeting of the Association for Research in Vision and Ophthalmology (ARVO 2017). The opinions expressed herein do not reflect those of the Department of Veteran Affairs, the National Institutes of Health, or the US Government.

AUTHOR CONTRIBUTIONS

S.R.R., S.J.F., and S.J.P. designed the study; D.A.S. and S.J.P. identified initial *Dhdds*$^{flx/flx}$ founders and verified FRT excision; S.R.R., L.A.S., M.C.B., F.W., A.O., L.S., G.S., and W.D. collected the data; S.J.F., S.J.P., S.R.R., E.S., X.M. interpreted the data; S.R.R. wrote the initial manuscript draft and generated the figures; S.J.F. and S.J.P. were primary editors of the manuscript. All persons listed as coauthors reviewed and contributed to editing of drafts of the manuscript contents and approved the final version before submission for publication.

DECLARATION OF INTERESTS

The authors declare no competing interests.

Received: February 18, 2020
Revised: April 10, 2020
Accepted: May 20, 2020
Published: June 26, 2020

REFERENCES

Adair, W.L., Jr., and Cafmeyer, N. (1987). Cell-cycle dependence of dolichyl phosphate biosynthesis. Arch. Biochem. Biophys. *258*, 491–497.

Ashida, H., Maeda, Y., and Kinoshita, T. (2006). DPM1, the catalytic subunit of dolichol-phosphate mannose synthase, is tethered to and stabilized on the endoplasmic reticulum membrane by DPM3. J. Biol. Chem. *281*, 896–904.

Atiskova, Y., Bartsch, S., Danyukova, T., Becker, E., Hagel, C., Storch, S., and Bartsch, U. (2019). Mice deficient in the lysosomal enzyme palmitoyl-protein thioesterase 1 (PPT1) display a complex retinal phenotype. Sci. Rep. *9*, 14185.

Behrens, N.H., and Leloir, L.F. (1970). Dolichol monophosphate glucose: an intermediate in glucose transfer in liver. Proc. Natl. Acad. Sci. U S A *66*, 153–159.

Biswas, P., Duncan, J.L., Maranhao, B., Kozak, I., Branham, K., Gabriel, L., Lin, J.H., Barteselli, G., Navani, M., Suk, J., et al. (2017). Genetic analysis of 10 pedigrees with inherited retinal degeneration by exome sequencing and phenotype-genotype association. Physiol. Genomics *49*, 216–229.

Brightman, D.S., Razafsky, D., Potter, C., Hodzic, D., and Chen, S. (2016). Nrl-Cre transgenic mouse mediates loxP recombination in developing rod photoreceptors. Genesis *54*, 129–135.

Buczkowska, A., Swiezewska, E., and Lefeber, D.J. (2015). Genetic defects in dolichol metabolism. J. Inherit. Metab. Dis. *38*, 157–169.

Burda, P., and Aebi, M. (1999). The dolichol pathway of N-linked glycosylation. Biochim. Biophys. Acta *1426*, 239–257.

Burton, W.A., Scher, M.G., and Waechter, C.J. (1979). Enzymatic phosphorylation of dolichol in central nervous tissue. J. Biol. Chem. *254*, 7129–7136.

Cantagrel, V., Lefeber, D.J., Ng, B.G., Guan, Z., Silhavy, J.L., Bielas, S.L., Lehle, L., Hombauer, H., Adamowicz, M., Swiezewska, E., et al. (2010). SRD5A3 is required for converting polyprenol to dolichol and is mutated in a congenital glycosylation disorder. Cell *142*, 203–217.

Carson, D.D., and Lennarz, W.J. (1981). Relationship of dolichol synthesis to glycoprotein synthesis during embryonic development. J. Biol. Chem. *256*, 4679–4686.

Carter-Dawson, L.D., and Lavail, M.M. (1979). Rods and cones in the mouse retina. I. Structural analysis using light and electron microscopy. J. Comp. Neurol. *188*, 245–262.

Chen, M., and Xu, H. (2015). Parainflammation, chronic inflammation, and age-related macular degeneration. J. Leukoc. Biol. *98*, 713–725.

Chojnacki, T., and Dallner, G. (1988). The biological role of dolichol. Biochem. J. *251*, 1–9.

Cusato, K., Ripps, H., Zakevicius, J., and Spray, D.C. (2006). Gap junctions remain open during cytochrome c-induced cell death: relationship of conductance to 'bystander' cell killing. Cell Death Differ. *13*, 1707–1714.

Defoe, D.M., Besharse, J.C., and Fliesler, S.J. (1986). Tunicamycin-induced dysgenesis of retinal rod outer segment membranes. II. Quantitative freeze-fracture analysis. Invest. Ophthalmol. Vis. Sci. *27*, 1595–1601.

Denecke, J., and Kranz, C. (2009). Hypoglycosylation due to dolichol metabolism defects. Biochim. Biophys. Acta *1792*, 888–895.

Devine, L., Lightman, S.L., and Greenwood, J. (1996). Role of LFA-1, ICAM-1, VLA-4 and VCAM-1 in lymphocyte migration across retinal pigment epithelial monolayers in vitro. Immunology *88*, 456–462.

Doucey, M.A., Hess, D., Cacan, R., and Hofsteenge, J. (1998). Protein C-mannosylation is enzyme-catalysed and uses dolichyl-phosphate-mannose as a precursor. Mol. Biol. Cell *9*, 291–300.

Doyle, J.W., and Kandutsch, A.A. (1988). Requirement for mevalonate in cycling cells: quantitative and temporal aspects. J. Cell Physiol. *137*, 133–140.

Endo, S., Zhang, Y.W., Takahashi, S., and Koyama, T. (2003). Identification of human dehydrodolichyl diphosphate synthase gene. Biochim. Biophys. Acta *1625*, 291–295.

Ferrari, S., Di Iorio, E., Barbaro, V., Ponzin, D., Sorrentino, F.S., and Parmeggiani, F. (2011). Retinitis pigmentosa: genes and disease mechanisms. Curr. Genomics *12*, 238–249.

Fliesler, S.J., and Basinger, S.F. (1985). Tunicamycin blocks the incorporation of opsin into retinal rod outer segment membranes. Proc. Natl. Acad. Sci. U S A *82*, 1116–1120.

Fliesler, S.J., Rapp, L.M., and Hollyfield, J.G. (1984a). Photoreceptor-specific degeneration caused by tunicamycin. Nature *311*, 575–577.

Fliesler, S.J., Tabor, G.A., and Hollyfield, J.G. (1984b). Glycoprotein synthesis in the human retina: localization of the lipid intermediate pathway. Exp. Eye Res. *39*, 153–173.

Fliesler, S.J., Rayborn, M.E., and Hollyfield, J.G. (1985). Membrane morphogenesis in retinal rod outer segments: inhibition by tunicamycin. J. Cell Biol. *100*, 574–587.

Gandini, R., Reichenbach, T., Tan, T.C., and Divne, C. (2017). Structural basis for dolichylphosphate mannose biosynthesis. Nat. Commun. *8*, 120.

Grabowska, D., Karst, F., and Szkopinska, A. (1998). Effect of squalene synthase gene disruption on synthesis of polyprenols in Saccharomyces cerevisiae. FEBS Lett. *434*, 406–408.

Guo, R.T., Ko, T.P., Chen, A.P., Kuo, C.J., Wang, A.H., and Liang, P.H. (2005). Crystal structures of undecaprenyl pyrophosphate synthase in complex with magnesium, isopentenyl pyrophosphate, and farnesyl thiopyrophosphate: roles of the metal ion and conserved residues in catalysis. J. Biol. Chem. *280*, 20762–20774.

Hageman, G.S., and Johnson, L.V. (1986). Biochemical characterization of the major peanut-agglutinin-binding glycoproteins in vertebrate retinae. J. Comp. Neurol. *249*, 499–510, 482-483.

Hamdan, F.F., Myers, C.T., Cossette, P., Lemay, P., Spiegelman, D., Laporte, A.D., Nassif, C., Diallo, O., Monlong, J., Cadieux-Dion, M., et al. (2017). High rate of recurrent de novo mutations in developmental and epileptic encephalopathies. Am. J. Hum. Genet. *101*, 664–685.

Hamel, C. (2006). Retinitis pigmentosa. Orphanet J. Rare Dis. *1*, 40.

Heesen, S., Lehle, L., Weissmann, A., and Aebi, M. (1994). Isolation of the ALG5 locus encoding the UDP-glucose:dolichyl-phosphate glucosyltransferase from Saccharomyces cerevisiae. Eur. J. Biochem. *224*, 71–79.

Iwabe, S., Ying, G.S., Aguirre, G.D., and Beltran, W.A. (2016). Assessment of visual function and retinal structure following acute light exposure in the light sensitive T4R rhodopsin mutant dog. Exp. Eye Res. *146*, 341–353.

Jakobsson, A., Swiezewska, E., Chojnacki, T., and Dallner, G. (1989). Uptake and modification of dietary polyprenols and dolichols in rat liver. FEBS Lett. *255*, 32–36.

Kaneko, H., Nishiguchi, K.M., Nakamura, M., Kachi, S., and Terasaki, H. (2008). Characteristics of bone marrow-derived microglia in the normal and injured retina. Invest. Ophthalmol. Vis. Sci. *49*, 4162–4168.

Kaushal, S., Ridge, K.D., and Khorana, H.G. (1994). Structure and function in rhodopsin: the role of asparagine-linked glycosylation. Proc. Natl. Acad. Sci. U S A *91*, 4024–4028.

Kean, E.L. (1977). The biosynthesis of mannolipids and mannose-containing complex glycans by the retina. J. Supramol Struct. *7*, 381–395.

Kean, E.L. (1980). The lipid intermediate pathway in the retina for the activation of carbohydrates involved in the glycosylation of rhodopsin. Neurochem. Int. *1C*, 59–68.

Kean, E.L. (1999). The dolichol pathway in the retina and its involvement in the glycosylation of rhodopsin. Biochim. Biophys. Acta *1473*, 272–285.

Kimchi, A., Khateb, S., Wen, R., Guan, Z., Obolensky, A., Beryozkin, A., Kurtzman, S., Blumenfeld, A., Pras, E., Jacobson, S.G., et al. (2018). Nonsyndromic retinitis pigmentosa in the Ashkenazi Jewish population: genetic and clinical aspects. Ophthalmology *125*, 725–734.

Krasnova, L., and Wong, C.H. (2016). Understanding the chemistry and biology of glycosylation with glycan synthesis. Annu. Rev. Biochem. *85*, 599–630.

Lam, B.L., Zuchner, S.L., Dallman, J., Wen, R., Alfonso, E.C., Vance, J.M., and Pericak-Vance, M.A. (2014). Mutation K42E in dehydrodolichol diphosphate synthase (DHDDS) causes recessive retinitis pigmentosa. Adv. Exp. Med. Biol. *801*, 165–170.

Larkin, M.A., Blackshields, G., Brown, N.P., Chenna, R., Mcgettigan, P.A., Mcwilliam, H., Valentin, F., Wallace, I.M., Wilm, A., Lopez, R., et al. (2007). Clustal W and clustal X version 2.0. Bioinformatics *23*, 2947–2948.

Larsson, O., and Wejde, J. (1992). Dolichol delays G1-arrest for one cell cycle in human fibroblasts subjected to depletion of serum or mevalonate. J. Cell Sci. *103* (Pt 4), 1065–1072.

Le, Y.Z., Zheng, L., Zheng, W., Ash, J.D., Agbaga, M.P., Zhu, M., and Anderson, R.E. (2006). Mouse opsin promoter-directed Cre recombinase expression in transgenic mice. Mol. Vis. *12*, 389–398.

Li, S., Chen, D., Sauve, Y., Mccandless, J., Chen, Y.J., and Chen, C.K. (2005). Rhodopsin-iCre transgenic mouse line for Cre-mediated rod-specific gene targeting. Genesis *41*, 73–80.

Ma, Y., Han, X., De Castro, R.B., Zhang, P., Zhang, K., Hu, Z., and Qin, L. (2018). Analysis of the bystander effect in cone photoreceptors via a guided neural network platform. Sci. Adv. *4*, eaas9274.

Maeda, Y., Tanaka, S., Hino, J., Kangawa, K., and Kinoshita, T. (2000). Human dolichol-phosphate-mannose synthase consists of three subunits, DPM1, DPM2 and DPM3. EMBO J. *19*, 2475–2482.

Mesri, M., Liversidge, J., and Forrester, J.V. (1994). ICAM-1/LFA-1 interactions in T-lymphocyte activation and adhesion to cells of the blood-retina barrier in the rat. Immunology *83*, 52–57.

Morava, E., Wosik, H.N., Sykut-Cegielska, J., Adamowicz, M., Guillard, M., Wevers, R.A., Lefeber, D.J., and Cruysberg, J.R. (2009). Ophthalmological abnormalities in children with congenital disorders of glycosylation type I. Br. J. Ophthalmol. *93*, 350–354.

Murray, A.R., Fliesler, S.J., and Al-Ubaidi, M.R. (2009). Rhodopsin: the functional significance of asn-linked glycosylation and other post-translational modifications. Ophthalmic Genet. *30*, 109–120.

Murray, A.R., Vuong, L., Brobst, D., Fliesler, S.J., Peachey, N.S., Gorbatyuk, M.S., Naash, M.I., and Al-Ubaidi, M.R. (2015). Glycosylation of rhodopsin is necessary for its stability and incorporation into photoreceptor outer segment discs. Hum. Mol. Genet. *24*, 2709–2723.

Ng, B.G., and Freeze, H.H. (2018). Perspectives on glycosylation and its congenital disorders. Trends Genet. *34*, 466–476.

Noailles, A., Kutsyr, O., Maneu, V., Ortuno-Lizaran, I., Campello, L., de Juan, E., Gomez-Vicente, V., Cuenca, N., and Lax, P. (2019). The absence of toll-Like receptor 4 mildly affects the structure and function in the adult mouse retina. Front Cell Neurosci *13*, 59.

Parentini, I., Cavallini, G., Donati, A., Gori, Z., and Bergamini, E. (2005). Accumulation of dolichol in older tissues satisfies the proposed criteria to be qualified a biomarker of aging. J. Gerontol. A. Biol. Sci. Med. Sci. *60*, 39–43.

Park, E.J., Grabinska, K.A., Guan, Z., and Sessa, W.C. (2016). NgBR is essential for endothelial cell glycosylation and vascular development. EMBO Rep. *17*, 167–177.

Park, E.J., Grabinska, K.A., Guan, Z., Stranecky, V., Hartmannova, H., Hodanova, K., Baresova, V., Sovova, J., Jozsef, L., Ondruskova, N., et al. (2014). Mutation of Nogo-B receptor, a subunit of cis-prenyltransferase, causes a congenital disorder of glycosylation. Cell Metab. *20*, 448–457.

Ramachandra Rao, S., Fliesler, S.J., Kotla, P., Nguyen, M.N., and Pittler, S.J. (2020). Lack of overt retinal degeneration in a K42E *Dhdds* knock-in mouse model of RP59. Cells *9*, 896.

Ripps, H. (2002). Cell death in retinitis pigmentosa: gap junctions and the 'bystander' effect. Exp. Eye Res. *74*, 327–336.

Rush, J.S., Cho, S.K., Jiang, S., Hofmann, S.L., and Waechter, C.J. (2002). Identification and characterization of a cDNA encoding a dolichyl pyrophosphate phosphatase located in the endoplasmic reticulum of mammalian cells. J. Biol. Chem. *277*, 45226–45234.

Sabry, S., Vuillaumier-Barrot, S., Mintet, E., Fasseu, M., Valayannopoulos, V., Heron, D., Dorison, N., Mignot, C., Seta, N., Chantret, I., et al. (2016). A case of fatal Type I congenital disorders of glycosylation (CDG I) associated with low dehydrodolichol diphosphate synthase (DHDDS) activity. Orphanet J. Rare Dis. *11*, 84.

Sakakihara, Y., and Volpe, J.J. (1984). Dolichol deposition in developing mammalian brain: content of free and fatty-acylated dolichol and proportion of specific isoprenologues. Brain Res. *316*, 255–262.

Schenk, B., Fernandez, F., and Waechter, C.J. (2001). The ins(ide) and out(side) of dolichyl phosphate biosynthesis and recycling in the endoplasmic reticulum. Glycobiology *11*, 61R–70R.

Shridas, P., and Waechter, C.J. (2006). Human dolichol kinase, a polytopic endoplasmic reticulum membrane protein with a cytoplasmically oriented CTP-binding site. J. Biol. Chem. *281*, 31696–31704.

Slijkerman, R.W., Song, F., Astuti, G.D., Huynen, M.A., Van Wijk, E., Stieger, K., and Collin, R.W. (2015). The pros and cons of vertebrate animal models for functional and therapeutic research on inherited retinal dystrophies. Prog. Retin. Eye Res. *48*, 137–159.

Sparks, S.E., and Krasnewich, D.M. (1993). Congenital disorders of N-linked glycosylation and multiple pathway overview. In GeneReviews((R)), M.P. Adam, H.H. Ardinger, R.A. Pagon, S.E. Wallace, L.J.H. Bean, K. Stephens, and A. Amemiya, eds. (University of Washington).

St Jules, R.S., Smith, S.B., and O'brien, P.J. (1990). The localization and timing of post-translational modifications of rat rhodopsin. Exp. Eye Res. *51*, 427–434.

Sullivan, L.J., Makris, G.S., Dickinson, P., Mulhall, L.E., Forrest, S., Cotton, R.G., and Loughnan, M.S. (1993). A new codon 15 rhodopsin gene mutation in autosomal dominant retinitis pigmentosa is associated with sectorial disease. Arch. Ophthalmol. *111*, 1512–1517.

Swiezewska, E., and Danikiewicz, W. (2005). Polyisoprenoids: structure, biosynthesis and function. Prog. Lipid Res. *44*, 235–258.

Thompson, D.A., Lyons, R.J., Liasis, A., Russell-Eggitt, I., Jagle, H., and Grunewald, S. (2012). Retinal on-pathway deficit in congenital disorder of glycosylation due to phosphomannomutase deficiency. Arch. Ophthalmol. *130*, 712–719.

Thompson, D.A., Lyons, R.J., Russell-Eggitt, I., Liasis, A., Jagle, H., and Grunewald, S. (2013). Retinal characteristics of the congenital disorder of glycosylation PMM2-CDG. J. Inherit. Metab. Dis. *36*, 1039–1047.

Ulshafer, R.J., Allen, C.B., and Fliesler, S.J. (1986). Tunicamycin-induced dysgenesis of retinal rod outer segment membranes. I. A scanning electron microscopy study. Invest. Ophthalmol. Vis. Sci. *27*, 1587–1594.

Van Den Born, L.I., Van Schooneveld, M.J., de Jong, L.A., Riemslag, F.C., de Jong, P.T., Gal, A., and Bleeker-Wagemakers, E.M. (1994). Thr4Lys rhodopsin mutation is associated with autosomal dominant retinitis pigmentosa of the cone-rod type in a small Dutch family. Ophthalmic Genet. *15*, 51–60.

Varner, H.H., Rayborn, M.E., Osterfeld, A.M., and Hollyfield, J.G. (1987). Localization of proteoglycan within the extracellular matrix sheath of cone photoreceptors. Exp. Eye Res. *44*, 633–642.

Volpe, J.J., Sakakihara, Y., and Rust, R.S. (1987). Dolichol kinase and the regulation of dolichyl phosphate levels in developing brain. Brain Res. *428*, 193–200.

Welply, J.K., Shenbagamurthi, P., Lennarz, W.J., and Naider, F. (1983). Substrate recognition by oligosaccharyltransferase. Studies on glycosylation of modified Asn-X-Thr/Ser tripeptides. J. Biol. Chem. *258*, 11856–11863.

Wen, R., Dallman, J.E., Li, Y., Züchner, S.L., Vance, J.M., Peričak-Vance, M.A., and Lam, B.L. (2014). Knock-down DHDDS expression Induces photoreceptor degeneration in zebrafish. In Retinal Degenerative Diseases. Advances in Experimental Medicine and Biology, *801*, J. Ash, C. Grimm, J.G. Hollyfield, R.E. Anderson, M.M.

LaVail, and C. Bowes Rickman, eds (Springer), pp. 543–550.

Wen, R., Lam, B.L., and Guan, Z. (2013). Aberrant dolichol chain lengths as biomarkers for retinitis pigmentosa caused by impaired dolichol biosynthesis. J. Lipid Res. *54*, 3516–3522.

Westphal, V., Kjaergaard, S., Schollen, E., Martens, K., Grunewald, S., Schwartz, M., Matthijs, G., and Freeze, H.H. (2002). A frequent mild mutation in ALG6 may exacerbate the clinical severity of patients with congenital disorder of glycosylation Ia (CDG-Ia) caused by phosphomannomutase deficiency. Hum. Mol. Genet. *11*, 599–604.

Williams, M.R., and Luscinskas, F.W. (2011). Leukocyte rolling and adhesion via ICAM-1 signals to endothelial permeability. Focus on "Leukocyte rolling and adhesion both contribute to regulation of microvascular permeability to albumin via ligation of ICAM-1". Am. J. Physiol. Cell Physiol. *301*, C777–C779.

Wong, T.K., and Lennarz, W.J. (1982). Biosynthesis of dolichol and cholesterol during embryonic development of the chicken. Biochim. Biophys. Acta *710*, 32–38.

Wu, X., Rush, J.S., Karaoglu, D., Krasnewich, D., Lubinsky, M.S., Waechter, C.J., Gilmore, R., and Freeze, H.H. (2003). Deficiency of UDP-GlcNAc:dolichol phosphate N-Acetylglucosamine-1 phosphate transferase (DPAGT1) causes a novel congenital disorder of glycosylation type Ij. Hum. Mutat. *22*, 144–150.

Xu, H., Chen, M., Mayer, E.J., Forrester, J.V., and Dick, A.D. (2007). Turnover of resident retinal microglia in the normal adult mouse. Glia *55*, 1189–1198.

Zelinger, L., Banin, E., Obolensky, A., Mizrahi-Meissonnier, L., Beryozkin, A., Bandah-Rozenfeld, D., Frenkel, S., Ben-Yosef, T., Merin, S., Schwartz, S.B., et al. (2011). A missense mutation in DHDDS, encoding dehydrodolichyl diphosphate synthase, is associated with autosomal-recessive retinitis pigmentosa in Ashkenazi Jews. Am. J. Hum. Genet. *88*, 207–215.

Zhao, L., Zabel, M.K., Wang, X., Ma, W., Shah, P., Fariss, R.N., Qian, H., Parkhurst, C.N., Gan, W.B., and Wong, W.T. (2015). Microglial phagocytosis of living photoreceptors contributes to inherited retinal degeneration. EMBO Mol. Med. *7*, 1179–1197.

Zhu, L., Jang, G.F., Jastrzebska, B., Filipek, S., Pearce-Kelling, S.E., Aguirre, G.D., Stenkamp, R.E., Acland, G.M., and Palczewski, K. (2004). A naturally occurring mutation of the opsin gene (T4R) in dogs affects glycosylation and stability of the G protein-coupled receptor. J. Biol. Chem. *279*, 53828–53839.

Zuchner, S., Dallman, J., Wen, R., Beecham, G., Naj, A., Farooq, A., Kohli, M.A., Whitehead, P.L., Hulme, W., Konidari, I., et al. (2011). Whole-exome sequencing links a variant in DHDDS to retinitis pigmentosa. Am. J. Hum. Genet. *88*, 201–206.

iScience, Volume *23*

Supplemental Information

Retinal Degeneration Caused by Rod-Specific *Dhdds* Ablation Occurs without Concomitant Inhibition of Protein *N*-Glycosylation

Sriganesh Ramachandra Rao, Lara A. Skelton, Fuguo Wu, Agnieszka Onysk, Grzegorz Spolnik, Witold Danikiewicz, Mark C. Butler, Delores A. Stacks, Liliana Surmacz, Xiuqian Mu, Ewa Swiezewska, Steven J. Pittler, and Steven J. Fliesler

SUPPLEMENTAL TABLES

ANTIBODY	***SOURCE/VENDOR***	***IDENTIFIER***
Anti-Opsin	Abcam	ab5417 RRID: AB_304874
Anti-GFAP	Dako Agilent	Z0334 RRID: AB_10013382
Anti-Iba1	Abcam	ab178846 RRID: AB_2636859
Anti-Cone Arrestin	Gift: Dr. Cheryl Craft USC, California, USA	PMID: 18701071
Anti-LAMP2	Abcam	ab13524 RRID: AB_2134736
Anti-GLUL	BD Biosciences	610517 RRID: AB_397879
Anti-ICAM1	R&D Systems	AF796
Anti-ACTB	Cell Signaling Technologies	4970 RRID: AB_2223172
Rabbit IgG	Sigma Aldrich	12-370
Mouse IgG	Sigma Aldrich	12-371
LECTIN	***SOURCE/VENDOR***	***IDENTIFIER***
Biotinylated Concanavalin-A	Vector Laboratories	B-1005 RRID: AB_2336346
AF647-Peanut Agglutinin	Thermo Fisher Scientific	L32460
AF647-Wheat Germ Agglutinin	Thermo Fisher Scientific	W32466
ASSAY	***SOURCE/VENDOR***	***IDENTIFIER***
PNGase-F Assay	New England Biolabs	P0704S
BaseScope ISH Assay	ACD Biotech	323900, 323910
Mouse Cytokine Assay	R&D Biosystems	ARY006
TUNEL Assay	Promega Corp.	G3250

Table S1. **Vendor information and identifiers for key reagents utilized in the study. Related to Figures 1 through 6 and Figures S1 through S13.**

TRANSPARENT METHODS

Materials and reagents

All reagents and materials utilized for SDS-PAGE and Western blot analyses were obtained from Bio-Rad Laboratories (Hercules, CA, USA). Other reagents were obtained from Sigma-Aldrich (St. Louis, MO, USA), unless otherwise stated. Plasticware (Falcon™) and all other general lab supplies were obtained from ThermoFisher Scientific (Waltham, MA, USA), unless otherwise indicated.

Generation of rod photoreceptor-specific DHDDS KO mouse

Two constructs containing lacZ flanked by FLP-FRT and *Dhdds* exon 3 flanked by loxP sites were obtained from the Knockout Mouse Project (Clones EPD0137_7_D05, EPD0137_7_D06; KOMP, UC Davis) and were linearized and introduced into mouse ES cells at the Roswell Park Comprehensive Cancer Center (RPCCC) Gene Targeting and Transgenic Facility (Buffalo, NY, USA) using standard technology. The lacZ cassette was excised from the established ES cells with FLP-FRT recombinase, and excision was confirmed by PCR with primers *Dhdds*-FWD: 5'-GTGTCATCCCCTGCTGCAGAT-3' and *Dhdds*-REV: 5'-TGGGTGTAGTGGCTCAGGTC-3', designed in a region that is conserved in both WT and floxed alleles and in the region around the loxP sites. PCR products amplified are 393 and 517 bp for the WT and floxed alleles, respectively. These primers were used to verify the presence of the *Dhdds*$^{flx/flx}$ alleles in all subsequent breedings. Verified Dhdds$^{flx/+}$ heterozygous mice were crossbred to generate homozygotes. In the Rho-iCre (iCre-75) mouse line, Cre recombinase transgene expression in rod photoreceptors is driven by the opsin (RHO) promoter (Li et al., 2005). *Dhdds*$^{flx/flx}$ mice were crossed with Rho-iCre (iCre-75) mice (Stock 015850, RRID: IMSR_JAX:015850, The Jackson Laboratory, Bar Harbor, MN, USA) to generate first filial generation (F1) rod photoreceptor-specific heterozygous

knockouts (Dhdds$^{flx/+}$ iCre^{+}), which were bred to homozygous *Dhdds*$^{flx/flx}$ mice to generate an F2 *Dhdds* knockout line that is homozygous for *the* floxed allele and heterozygous for iCre (*Dhdds*$^{flx/flx}$ iCre^{+}). PCR verification of Cre transgene modification was carried out using forward and reverse primers, 5'-TCAGTGCCTGGAGTTGCG-CTGTGG-3' and 5'-CTTAAAGGCCAGGGCCTGCTTGGC-3' yielding a 650 bp product. The PCR assay for Cre-recombinase does not differentiate between homozygous and heterozygous transgenic mice. For the PCR assay involving direct tissue genotyoping, primers [FWD: 5'-GTGTCATCCCCTGCT-GCAGAT-3', REV: 5'-GTGAAACAAGAACCATTTACCT-3'] were designed upstream of the upstream loxP site, and downstream of downstream loxP site [**Fig. 2**], predicted to yield a specific 584 bp remnant intronic region (due to exon 3 excision). Primers were designed to amplify an unaltered gene loci (*Dhcr7)* as a positive control using the following primer set: FWD 5' – CCCTAGTCACAACTTATGGCCCTT – 3', and REV 5' – TAGTTCCCACAGGTGACATTA – 3', which generates a 375 bp product

Rod-photoreceptor-specific expression and activity of Cre-recombinase in Rho-iCre75 mice was verified by breeding the mouse line to ZsGreen reporter mouse strain (B6.Cg-Gt(ROSA)26Sortm6(CAG-ZsGreen1)Hze/J, Stock# 007906, RRID: IMSR_JAX:007906; The Jackson Laboratory). The first filial, iCre^{+} progeny of the cross would yield ZsGreen expression exclusively in Cre recombinase-expressing cell types, by deleting the loxP sites flanking the STOP codon upstream of the ZsGreen gene.

Animals were maintained on a 12-h light:12-h dark cyclic light schedule (20-40 lux ambient light intensity at cage level), at 22-25°C, and typically were sacrificed 6 h into the light phase. All procedures conformed to the National Research Council's *Guide for the Care and Use of Laboratory Animals* (https://grants.nih.gov/grants/olaw/Guide-for-the-Care-and-use-of-laboratory-animals.pdf).

PCR and mutation verification

Genomic DNA from mouse tail snips was extracted using a Proteinase K-based method (Malumbres et al., 1997). Briefly, mouse tail snips were incubated for 4 h at 55°C in All^{ele}-In-One™ Mouse Tail Direct PCR buffer (Allele Biotechnology, San Diego, CA, USA; ABP-PP-MT01500). The one-step reaction makes the tail genomic DNA available for PCR amplification without purification. PCR amplification was performed using GreenTaq® DNA Polymerase (Sigma-Aldrich, S4438), and the MyIQ™ Single Color Real-Time PCR Detection System (Bio-Rad Laboratories; 170-9740) with cycles of 95ºC denaturation. Extension period for indirect and direct (tail snip and retina) genotyping was 45s at 54°C. The PCR products obtained using the primers described above were electrophoretically separated in a 1.5% agarose gel and stained with EtBr to verify product size, in comparison with a DNA size standard (ThermoFisher Scientific, 15628019), and visualized using a FOTODYNE FOTO/UV® 21 Transilluminator (FOTODYNE Inc.).

SDS-PAGE, Western blot and densitometric analyses

Retinas from age-matched WT and *Dhdds*$^{flx/flx}$ iCre^{+} mice were harvested, and flash frozen immediately. Retinas were lysed with RIPA buffer (ThermoFisher Scientific, 89900) supplemented with protease inhibitor cocktail (ThermoFisher Scientific, 78441) at 1:100 dilution. Protein yield was estimated using a Pierce™ BCA Protein Assay Kit (ThermoFisher Scientific, 23225). Western blot analysis was performed essentially as described previously (Ramachandra Rao et al., 2018), utilizing the following antibodies: mouse anti-opsin monoclonal antibody (Abcam, Burlingame, CA, USA; ab5417, RRID: AB_304874; 1:2000); rat anti-LAMP2 (Abcam, ab13524, RRID: AB_2134736; 1:1000); mouse anti-GLUL [BD Biosciences, San Jose, CA, USA; 610517, RRID: AB_397879; 1:1000], goat anti-ICAM-1 [R&D Systems, Minneapolis, MN, USA, AF796; 1:1000),

rabbit anti-ACTB (Cell Signaling Technology, Danvers, MA, USA; 4970, RRID: AB_2223172; 1:1000), and rabbit anti-GFAP (Dako Agilent, Sanata Clara, CA, USA; Z0334; 1:1000). Blots were then probed with appropriate host-specific alkaline phosphatase-tagged secondary antibodies (1h at room temperature). Detection of antibody binding was achieved using chemifluorescent enzyme substrate (GE Healthcare Life Sciences, Marlborough, MA, USA; 45000947) and a ChemiDoc™ MP Imaging System (Bio-Rad Laboratories). Semi-quantitative densitometry was performed using BioRad ImageLab® software.

Immunohistochemistry, on-section PNGase-F assay, and confocal microscopy

Eyes from WT and *Dhdds*-knockout animals were enucleated (6 h post light onset), fixed in 4% (w:v) formaldehyde (prepared from paraformaldehyde; Electron Microscopy Sciences, Hatfield, PA, USA; 30525-89-4)) in PBS on ice overnight, and then rinsed in chilled PBS three times. Fixed eyes were paraffin embedded, and 10-µm thick sections were collected onto glass Gold Seal™ UltraFrost™ microscope slides. The sections were de-paraffinized and antigen retrieval was carried out as described previously (Emoto et al., 2005). Immunohistochemistry was performed as described previously (Ramachandra Rao et al., 2018) using the following antibodies: mouse anti-opsin (Abcam, RRID: AB_304874; 1:200); rabbit anti-GFAP (Dako Agilent, Z0334, RRID: AB_10013382, 1:100); anti-Iba-1 (Abcam, ab178846, RRID: AB_2636859; 1:100); rabbit anti-cone arrestin (kind gift by Dr. Cheryl Craft, University of South California, USA). Negative controls consisted of nonimmune IgG (10 µg/ml) (Sigma-Aldrich; rabbit: 12-370, mouse: 12-371): from the same host species as that from which the primary antibody was derived. After three rinses with TBST (Tris-buffered saline, containing 0.2% (v/v) Tween-20), tissue sections were incubated for 45 min at room temperature with secondary IgG from suitable host species, conjugated with Alexa Fluor® 488/568/647 (1:500 in antibody diluent; ThermoFisher).

On-section PNGase-F *N*-glycosidase assay (New England Biolabs Inc., Ipswich, MA, USA; P0704S) was carried out as per manufacturer's instructions. Briefly, each retinal section was treated with 200 U of PNG-ase F in 1X Glycobuffer 2 (10X buffer provided with the kit) supplemented with 1% NP-40 detergent at 37^{O}C, overnight. WT and *Dhdds*$^{flx/flx}$ iCre^{+} retinal sections ± PNGase-F were incubated with biotinylated Concanavalin-A (Vector Laboratories, Burlingame, CA, USA: B-1005, RRID: AB_2336346; 1:100), followed by incubation with AF488-conjugated streptavidin (Thermo Fisher Scientific, S11223) and AF647-conjugated Peanut Agglutinin (Thermo Fisher Scientific, L32460). AF647-conjugated Wheat germ agglutinin (Thermo Fisher Scientific, W32466) was utilized to test the synthesis of glycans containing N-acetyl-D-glucosamine.

Slides were rinsed with TBS, counterstained with DAPI (4',6-diamido-2-phenylindole), coverslip mounted using Vectashield® mounting medium (Vector Laboratories, Burlingame, CA; H-1000), and examined with a Leica TCS SPEII DMI4000 scanning laser confocal fluorescence microscope (Leica Microsystems, Buffalo Grove, IL). Images were captured using a 40X oil immersion (RI-1.518) objective under nominal laser intensity (10% of maximum intensity), gain (850) and offset (-0.5) values, to optimize the signal-to-noise ratio.

In Situ Hybridization (ISH)

For the purpose of morphologic verification of successful deletion of exon 3 of *Dhdds*, we utilized an ISH methodology called BaseScope™ (ACDBio, CA, USA). Two sets of short 50 bp complimentary probes (which bind to the target mRNA, spanning a total of ~100bp), conventionally called "ZZ probes", were custom-designed to detect transcript region corresponding to *Dhdds* exon 3 (bp 361-455 of NM_026144.4). ISH was performed according to manufacturer instruction protocol (ACDBio, 323910 and 323900). High signal/noise ratio enables

visualization of specific stretches of the *Dhdds* target mRNA (in this case, *Dhdds)* as a single red chromogenic dot. Corresponding brightfield images were captures using Nikon 80i Fluorescence Microscope equipped with a digital camera and Image Pro analysis software (Nikon Instruments Inc., New York, USA)

Spectral Doman Optical Coherence Tomography (SD-OCT) analysis

All mice were maintained under a 12:12 light/dark cycle, at 20-40 Lux ambient room illumination. Overall retinal morphology and ONL thickness were periodically monitored and recorded non-invasively in age-matched C57BL/6J control and *Dhdds*$^{flx/flx}$ iCre^{+} mice, using a Bioptigen 840 nm UHR-SD-OCT instrument (Bioptigen, NC, USA) essentially as described previously (Butler and Sullivan, 2018). Mice were anesthetized using ketamine-xylazine (75 mg/kg-5 mg/kg) by intraperitoneal injection. Both pupils were dilated using 1% Atropine (Acorn Inc., NDC 17478-215-05). Following dilation, mice were positioned into the instruments AIM-RAS (animal imaging mount and rodent alignment stage) positioning setup, which allows for proper alignment of the mouse eye with the mouse retina bore. Horizontal SD-OCT scans (1.4 mm) were acquired, and B-scan cross-sectional images were analyzed. The image resolution allowed accurate determination of the integrity of the ONL and other retinal layers. The total ONL thickness was defined as the hyporeflective layer observed between the hyper-reflective OS and hyper-reflective OPL. ONL thickness around the optic nerve head (ONH) was measured in control and *Dhdds*$^{flx/flx}$ iCre^{+} mice, at PN 4, 5 and 6 weeks (n=4/group), utilizing Bioptigen InVivoVue® Clinic software. Layer thicknesses were measured manually. The measured ONL thickness was plotted as a function of distance from the ONH, and for statistical analysis one-way ANOVA was performed within GraphPad Prism® software (GraphPad Software, San Diego, CA, USA; RRID: SCR_002798).

Electron microscopy

Mouse eyes were processed for plastic embedment ultramicrotomy, and EM analysis as described in detail previously (Fliesler et al., 2004). In brief, a slit was made in the superior cornea with a razor blade and the eyes were fixed overnight at 4°C in fresh Karnovsky's fixative (0.125 M sodium cacodylate buffer (pH 7.4), containing 2.5% (v/v) glutaraldehyde, 2.0% formaldehyde and 0.025% $CaCl_2$). The fixed eyes were then rinsed with 0.1 M sodium cacodylate buffer (pH 7.4) containing 0.025% $CaCl_2$, and post-fixed for 1 h in 1% (w/v) osmium tetroxide in 0.1 M sodium cacodylate buffer. After post-fixation, the eyes were rinsed twice in 0.1 M sodium cacodylate buffer and once in distilled water, then dehydrated using a graded ethanol series followed by propylene oxide and infiltrated overnight with Spurr's epoxy resin (Spurr Low Viscosity Embedding Kit; Sigma-Aldrich, EM0300-1KT). The eyes were then embedded in Spurr's resin and allowed to polymerize in a 70°C oven for 48 h. Tissue sections were obtained with an ultramicrotome (UltraCut-E; Reichert Technologies Life Sciences, NY, USA) using glass or diamond knives. Thin (70- to 80-nm thickness) sections were collected on copper 75/300 mesh grids and stained with 2% (v/v) uranyl acetate and Reynolds' lead citrate. Sections were viewed and micrographs obtained with a JEOL Model 100CX electron microscope (JEOL, USA; Peabody, MA, USA) at an accelerating voltage of 60 keV

Electroretinography (ERG)

Scotopic (dark-adapted) electroretinograms were recorded from control C57BL/6J and *Dhdds*$^{flx/flx}$ iCre^{+} mice after overnight dark adaptation. Animals were anesthetized by intraperitoneal injection of a ketamine-xylazine mixture, followed by pupil dilation with an ophthalmic Atropine solution. Flash stimuli were applied using a ColorDome system (DiagnoSys LLC, Lowell, MA, USA). The ERGs were recorded from both eyes simultaneously using DTL thread contact electrodes

(OcuScience®, Henderson, NV, USA), contacting the corneal surface with a conductive medium (Goniovisc® (hydroxypropylmethylcellulose 2.5%), Hub Pharmaceuticals, 17238061015-EA). A bite bar and a platinum electrode under the skin served as reference and ground leads, respectively. Scotopic responses were obtained in 16 increasing flash intensity steps (10^{-3} to 500 cd-sec/m^2). Individual scotopic a-wave and b-wave responses for each strain examined were averaged (n=7-12). Individual b:a wave ratios were calculated at all flash intensities ≥1.25 cd-sec/m^2, and group averages and standard errors were calculated (n=7-12). Following rod desensitization achieved by maintaining a constant background illumination, photopic (light-adapted) ERG responses were elicited with green light (520 nm) flicker illumination at 30 Hz, using an 8-step custom protocol with increasing flash intensities (10^{-1} to 30 cd-sec/m^2). Statistical analysis using one-way ANOVA and Student's *t*-test were performed on data acquired at individual flash intensities, using GraphPad® software.

TUNEL assay

To visualize cell death, the *in situ* fluorescence-based Terminal deoxynucleotidyl transferase dUTP nick end labeling (TUNEL) assay (for detection of apoptotic cell death) was utilized as described previously (Tu et al., 2013). Paraffin sections of control and *Dhdds*$^{flx/flx}$ iCre^{+} eyes were deparaffinized, and citrate buffer antigen retrieval was performed. Sections were subjected to TUNEL assay, using a DeadEnd™ Fluorometric TUNEL System (G3250; Promega Corporation, Madison, WI, USA), per the manufacturer's instructions. Permeabilized sections were treated with equilibration buffer (provided by manufacturer), followed by Terminal Deoxynucleotidyl Transferase (TdT) labeling for one hour at 37^0C. Labeling reaction was halted by incubating in SSC Stop Buffer (provided by manufacturer) for 15 min. Sections were quickly rinsed three times in PBS and immunohistochemistry using Iba-1 monoclonal antibodies (Abcam, Cat. #ab178846; 1:100, RRID: AB_2636859) was performed as described above. Sections were DAPI stained, and

mounted using Vectashield® mounting medium (Vector Laboratories). Confocal fluorescence micrograph images were captured using the 488 nm wavelength channel to detect TUNEL-positive cells.

PNGase-F assay

Retinas from PN 5-week-old wild type and *Dhdds*$^{flx/flx}$ iCre^{+} retina were isolated and lysed in SDS-free homogenization buffer (SDS interferes with PNGase-F activity). After protein quantification using BCA assay (see Western blot section, above), 50 µg of protein was subjected to non-denaturing PNGase-F assay (New England Biolabs Inc., P0704S) as per manufacturer's instructions. Briefly, the protein sample (50 µg) was treated with 2,500 U of PNG-ase F in 1X Glycobuffer (10X buffer provided with the kit) supplemented with 1% NP-40 detergent at 37^{O}C, overnight. PNGase-F-treated WT and *Dhdds*$^{flx/flx}$ iCre^{+} retinal protein extract were compared with untreated extract by Western blot analysis, probing the blots with anti-RHO antibody (see pertinent section above)

Cytokine Array

An unbiased, broad screening approach was utilized to test the upregulation of cytokines in the observed retinal degeneration. For this purpose, a membrane-based sandwich assay [Proteome Profiler Mouse Cytokine Array Kit, R&D Systems, Minneapolis, MN, USE; ARY006] was adapted as per manufacturer's instructions.PN 5 week old *Dhdds*$^{flx/flx}$ iCre^{+} and *Dhdds*$^{flx/flx}$ iCre^{-} retinal protein extract (n=3/group; 200 µg of protein extract/array) were mixed with a cocktail of biotinylated detection antibodies (kit content), and subsequently incubated with the mouse cytokine array membrane. The membrane was washed, and incubated with streptavidin-horseradish peroxidase for 1 h. Femto Chemiluminescence detection system (ThermoFisher,

34094) was used for signal amplification, and array imaging/signal detection was carried out on a BioRad ChemiDoc™ MP Imaging System. Background noise was subtracted from the cytokine-specific signal utilizing ImageLab software, and background-corrected signal ratio between *Dhdds*$^{flx/flx}$ iCre^{+} and *Dhdds*$^{flx/flx}$ iCre^{-} was calculated for individual cytokines.

Analysis of dolichol content

Five retinas were pooled and subjected to alkaline hydrolysis at 95°C for 1 h in hydrolytic solution (25% (w/v) KOH in 65% (v/v) ethanol, *aq.*). Nonsaponifiable lipids were then extracted three times with hexane, pooled extracts were evaporated to dryness under a stream of nitrogen, and the residue was dissolved in 2-propanol. UHPLC-ESI-HR-MS analyses of polyisoprenoids were performed by the method described in detail previously (Jozwiak et al., 2017), using an ACQUITY I-Class Ultra-Performance Liquid Chromatograph (Waters Corporation, Milford, MA, USA) coupled with a Synapt G2-S HDMS mass spectrometer (Waters) equipped with an electrospray ion source and quadrupole time-of-flight (q-TOF) mass analyzer. The chromatographic separation of polyisoprenoids was carried out using an Acquity BEH C18 column (2.1 x 100 mm, 1.7 µm) (Waters). Mass spectra of polyisoprenoid alcohols were recorded in the positive ion mode with the resolving power of a TOF analyzer 20000 FWHM. The exact mass measurements for all peaks were performed within 3 mDa mass error. The instrument was controlled and recorded data were processed using a MassLynx V4.1 software package (Waters).

SUPPLEMENTAL REFERENCES

BUTLER, M. C. & SULLIVAN, J. M. 2018. Ultrahigh Resolution Mouse Optical Coherence Tomography to Aid Intraocular Injection in Retinal Gene Therapy Research. *J Vis Exp*.

EMOTO, K., YAMASHITA, S. & OKADA, Y. 2005. Mechanisms of heat-induced antigen retrieval: does pH or ionic strength of the solution play a role for refolding antigens? *J Histochem Cytochem,* 53**,** 1311-21.

FLIESLER, S. J., PEACHEY, N. S., RICHARDS, M. J., NAGEL, B. A. & VAUGHAN, D. K. 2004. Retinal degeneration in a rodent model of Smith-Lemli-Opitz syndrome: electrophysiologic, biochemical, and morphologic features. *Arch Ophthalmol,* 122**,** 1190-200.

JOZWIAK, A., LIPKO, A., KANIA, M., DANIKIEWICZ, W., SURMACZ, L., WITEK, A., WOJCIK, J., ZDANOWSKI, K., PACZKOWSKI, C., CHOJNACKI, T., POZNANSKI, J. & SWIEZEWSKA, E. 2017. Modeling of Dolichol Mass Spectra Isotopic Envelopes as a Tool to Monitor Isoprenoid Biosynthesis. *Plant Physiol,* 174**,** 857-874.

LI, S., CHEN, D., SAUVE, Y., MCCANDLESS, J., CHEN, Y. J. & CHEN, C. K. 2005. Rhodopsin-iCre transgenic mouse line for Cre-mediated rod-specific gene targeting. *Genesis,* 41**,** 73-80.

MALUMBRES, M., MANGUES, R., FERRER, N., LU, S. & PELLICER, A. 1997. Isolation of high molecular weight DNA for reliable genotyping of transgenic mice. *Biotechniques,* 22**,** 1114-9.

RAMACHANDRA RAO, S., PFEFFER, B. A., MAS GOMEZ, N., SKELTON, L. A., KEIKO, U., SPARROW, J. R., ROWSAM, A. M., MITCHELL, C. H. & FLIESLER, S. J. 2018. Compromised phagosome maturation underlies RPE pathology in cell culture and whole animal models of Smith-Lemli-Opitz Syndrome. *Autophagy***,** 1-22.

TU, C., LI, J., JIANG, X., SHEFLIN, L. G., PFEFFER, B. A., BEHRINGER, M., FLIESLER, S. J. & QU, J. 2013. Ion-current-based proteomic profiling of the retina in a rat model of Smith-Lemli-Opitz syndrome. *Mol Cell Proteomics,* 12**,** 3583-98.

SUPPLEMENTAL FIGURES

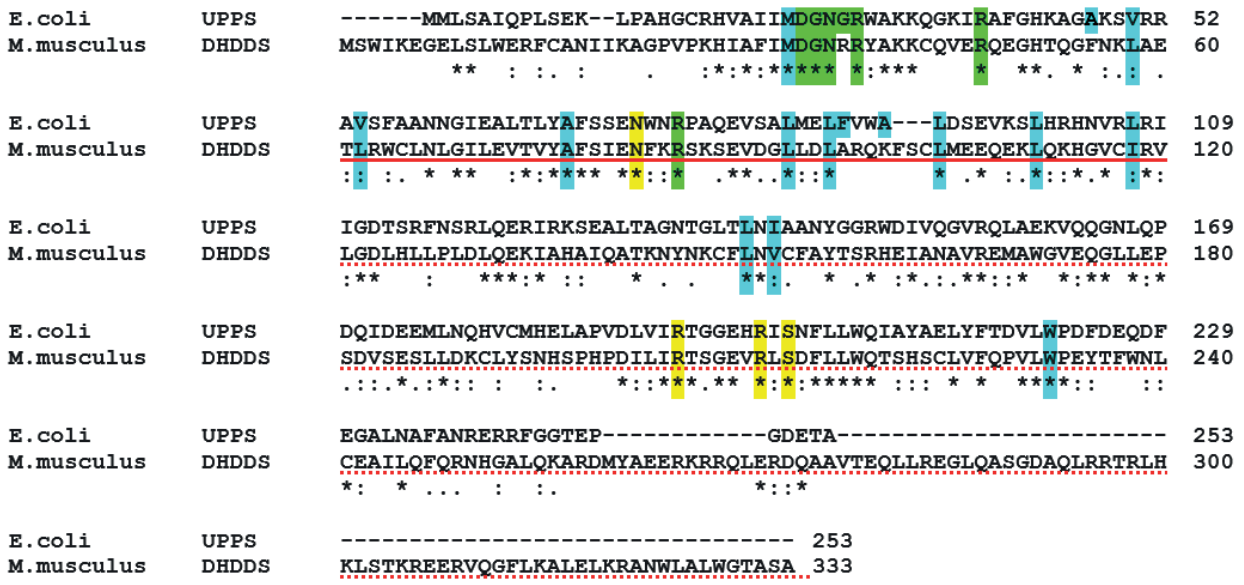

Figure S1. Multiple sequence alignment and comparison of FPP and IPP binding sites in the DHDDS complex. Related to Figure 1.

DHDDS is required for FPP and IPP condensation to generate polyprenol. Sequence alignment of murine (*M. musculus*) Dhdds against *E. coli* UPPS suggests conservation of critical amino acids required for FPP and IPP binding (*yellow, green highlights*), and hydrophobic interactions (*cyan highlights*). The conserved region required for FPP/IPP bindng is lost upon Cre-mediated excision of exon 3 of *Dhdds* (*solid red underline* corresponds to the region coded by exon 3; *dashed red underline* represents the peptide coded by downstream exons, which may not be translated due to the frameshift generated by deletion of exon 3). Notations: fully conserved (*); mostly conserved (**:**); partially conserved (**.**).

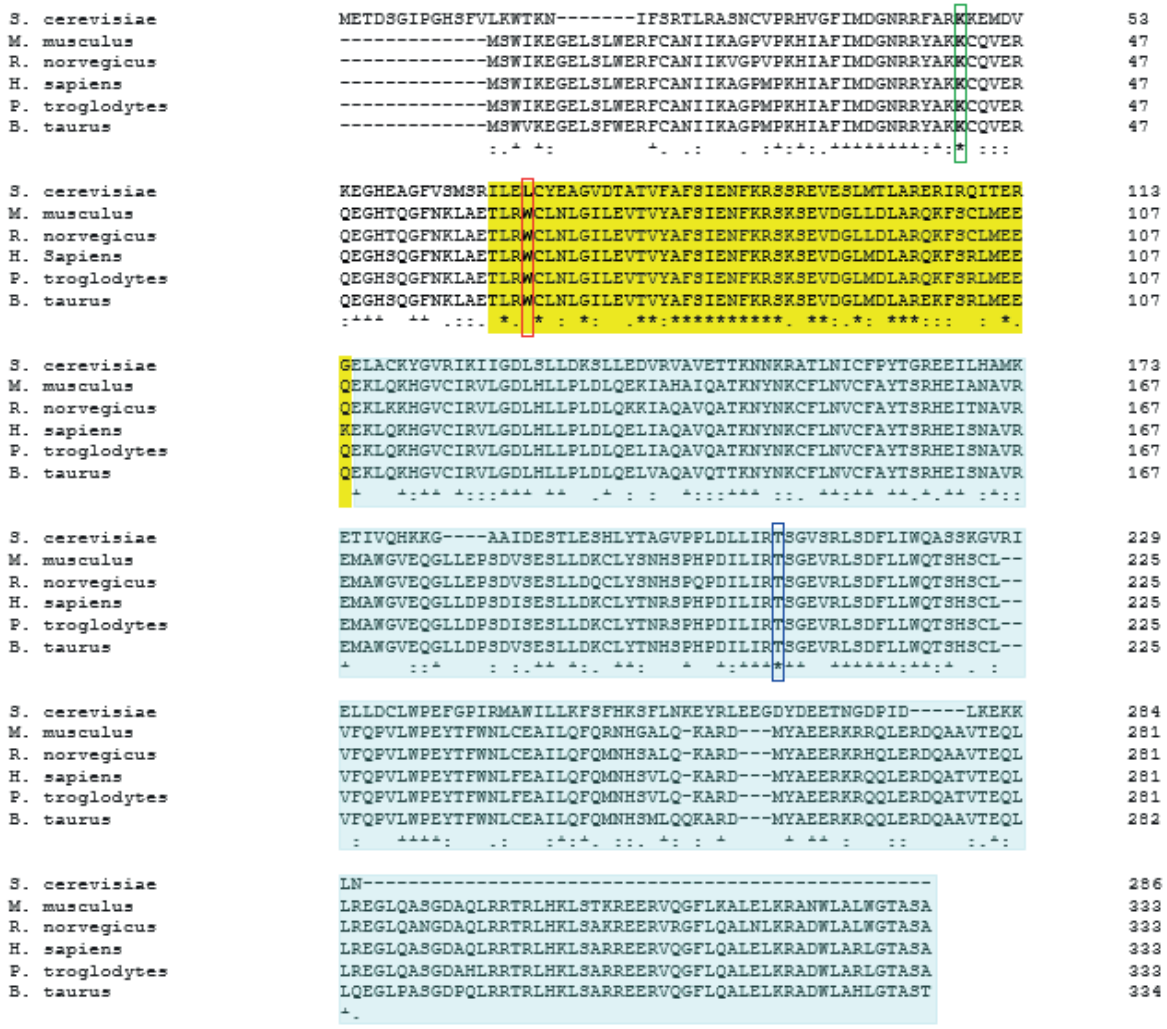

Figure S2. Multiple sequence alignment reveals species conservation of DHDDS FPP/IPP binding sites at the protein level. Related to Figure 1.

The peptide region coded by murine exon 3 of *Dhdds* (the targeted exon in this study, highlighted in *yellow*) is required for FPP binding, and is very well conserved between species. Critical FPP and IPP binding sites coded by exon 3 and downstream exons are highly conserved (see **Figure S1**). Known RP-associated DHDDS point mutations (K42E [*green box*], W64X [*red box*], T204A [*blue box*]) are shown. Downstream exons, which may not be translated due to the frameshift generated by deletion of exon 3, have been highlighted in cyan. Notations: fully conserved (*); mostly conserved (**:**); partially conserved (**.**).

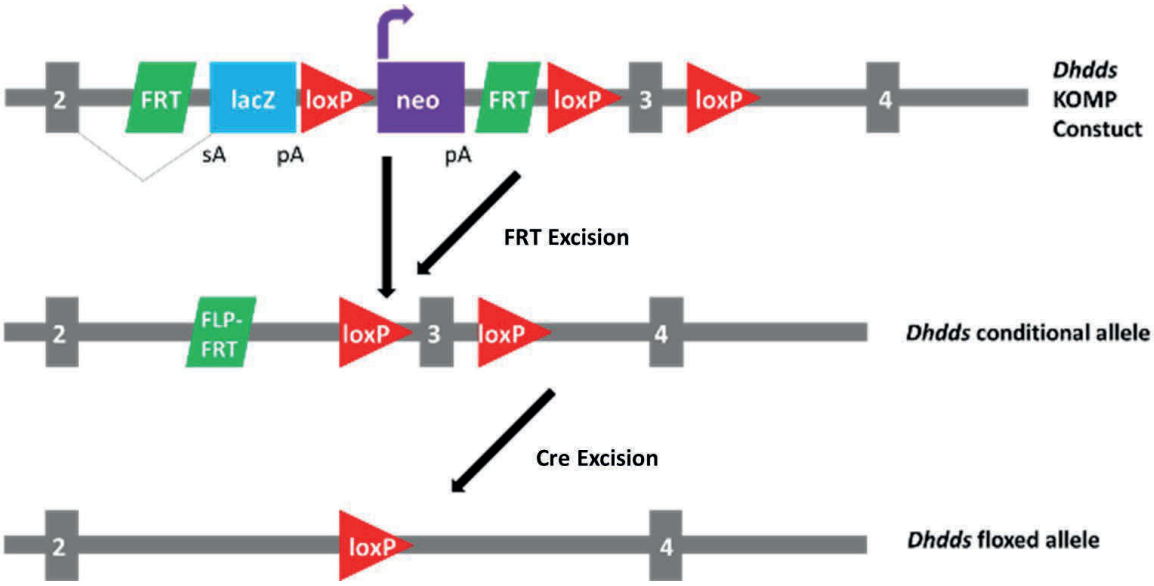

Figure S3. Knockout Mouse Project (KOMP) DHDDS conditional knockout alleles. Related to Figure 2.

A validated *Dhdds* plasmid construct was obtained from KOMP (U.C. Davis; Davis, CA, USA). The plasmid was linearized and introduced into mouse C57BL/6J mouse ES cells. Transformed cells were treated with FLP recombinase to excise the lacZ cassette, leaving a single FRT site. Confirmed FRT-excised ES cells were used to generate *Dhdds*$^{flx/flx}$ mice containing two loxP sites surrounding exon 3. Expression of Cre recombinase leads to excision of all sequence between the two loxP sites including all of exon 3, leaving behind a single loxP site.

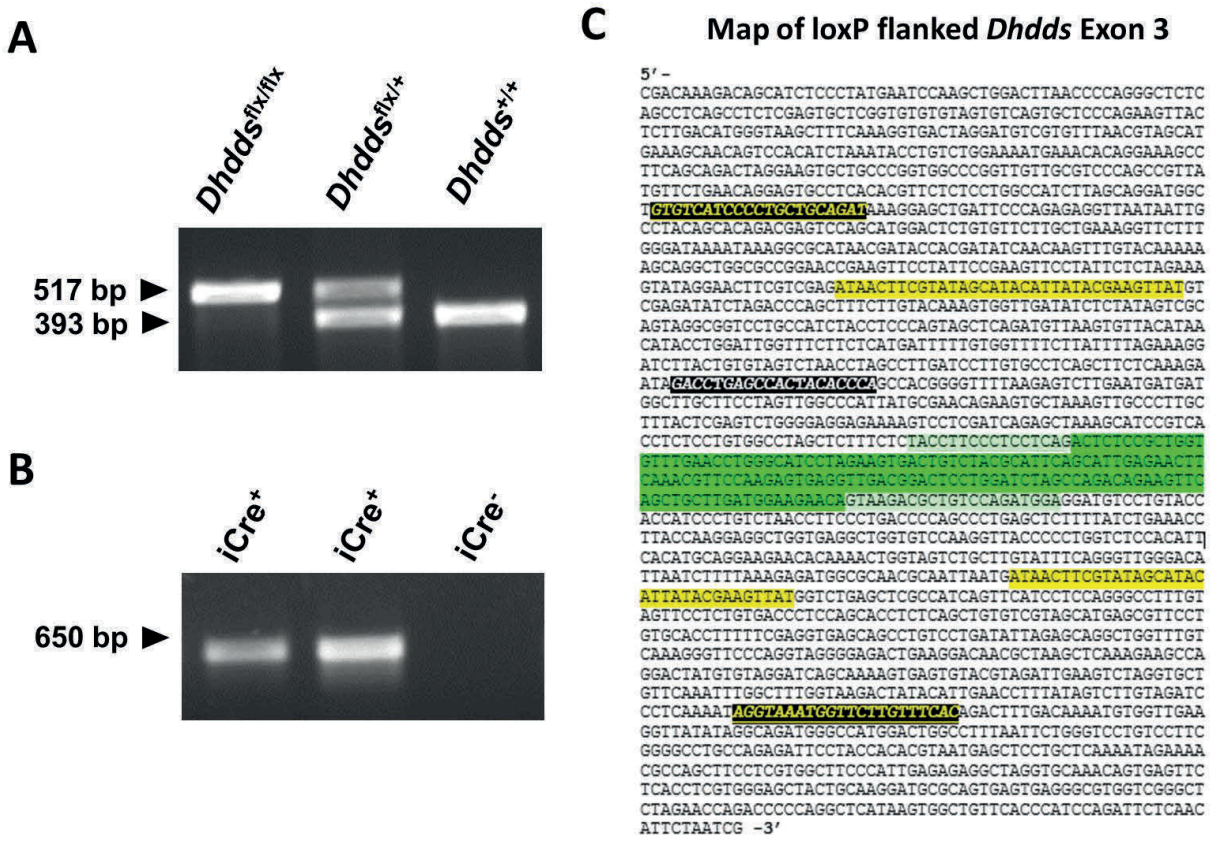

Fig. S4. Representative agarose gel image of initial PCR genotyping analysis using tail snip. Related to Figure 1.

A. Genomic DNA extracted from tail snips of *Dhdds*$^{flx/flx}$ iCre^{+}, *Dhdds*$^{flx/+}$ iCre^{+}, and *Dhdds*$^{+/+}$ iCre^{-} mice was subjected to PCR genotyping to differentiate the floxed *vs*. wild type alleles, as well as Cre recombinase status. The *Dhdds* WT allele yields a 393 bp product, while the *Dhdds* floxed allele yields a 517 bp product. **B.** PCR genotyping for the Rho- iCre allele. The Rho-iCre transgene yields a 650 bp product. **C.** The gene sequence of the loxP-modified *Dhdds* allele is shown, along with the PCR genotyping strategy and primer choices for tail snip and retinal genotyping (see **Figure 1**). The intronic region is highlighted in *cyan*, *Dhdds e*xon 3 is highlighted in *green*, upstream and downstream loxP sites are highlighted in *yellow*. Forward and reverse primers used in retinal genotyping are shown (*yellow text, black highlight*). Tail snip genotyping utilized the same forward primer as used for retinal genotyping; reverse primer for tail snip genotyping is shown (*white text, black highlight*).

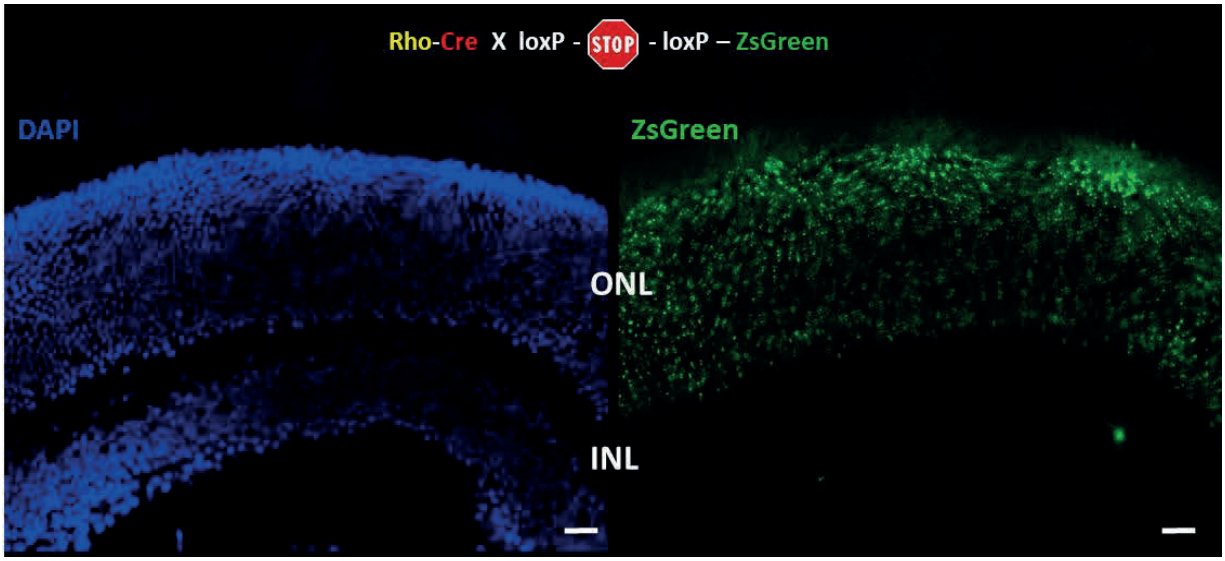

Figure S5. Cre recombinase activity is present in the majority of rod photoreceptors by PN 15 days. Related to Figure 2.

ZSgreen expression is exclusively expressed in rods, suggesting Rho-iCre activity. DAPI and GFP channels are shown separately to demonstrate ZsGreen expression exclusively in the majority of cells in the photoreceptor layer (~97% of which are rods) at PN 15 days. (See **Figure 2** for ZsGreen expression at PN 30 days.) [Scale bar: 20 μm.]

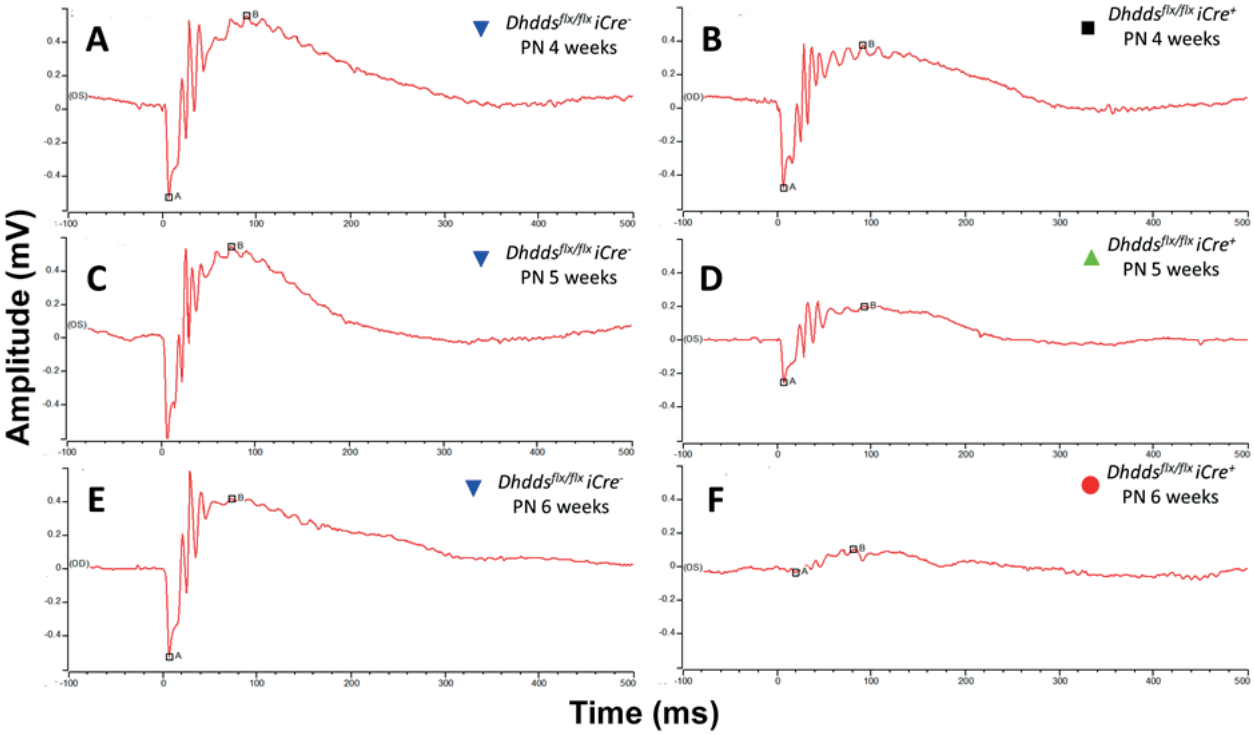

Figure S6. Representative scotopic ERG traces of age-matched *Dhdds*$^{flx/flx}$ iCre^{-} and *Dhdds*$^{flx/flx}$ iCre^{+} mice. Related to Figure 3.

Representative ERG traces of *Dhdds*$^{flx/flx}$ iCre^{+} mice (**B,D,F**) at highest flash intensity (500 cd-s/m^2) suggests rapid, age-related decline in scotopic response, compared to *Dhdds*$^{flx/flx}$ iCre^{-} mice (**A,C,E**), as observed in **Figure 3**. Scotopic ERG response in *Dhdds*$^{flx/flx}$ iCre^{+} mice were essentially extinguished by PN 6 weeks.

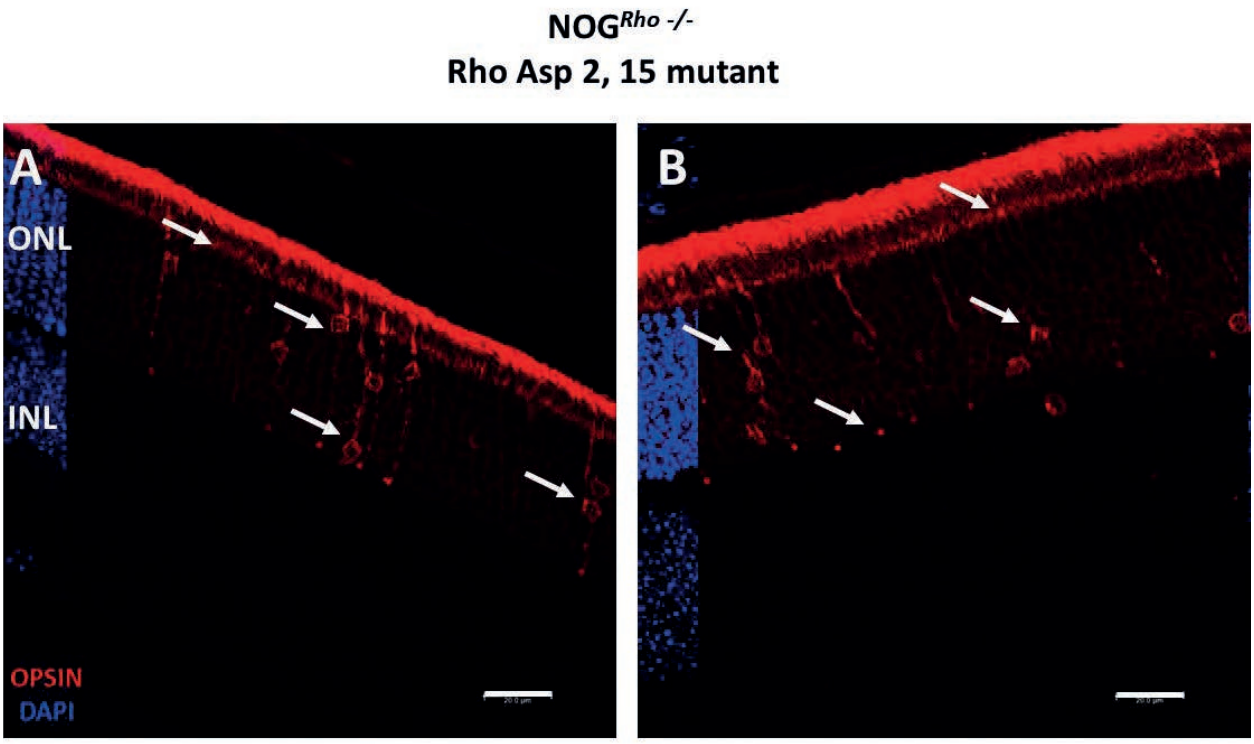

Figure S7. Demonstration of opsin trafficking defect in an established hypoglycosylation model. Related to Figure 5.
Immunohistochemistry using anti-opsin antibody to localize rhodopsin in the Nog$^{Rho-/-}$ mouse retina (a positive control for opsin hypoglycosylation) demonstrates defective intracellular trafficking of opsin. Opsin mislocalization leads to IS (*arrows*) and perinuclear (*arrowheads*) accumulation. DAPI staining (*blue*) is shown on the left-hand side of each micrograph. This is in agreement with the lack of obvious *N*-glycosylation defects observed in **Figure 5.** [Scale bar: 20 μm.]

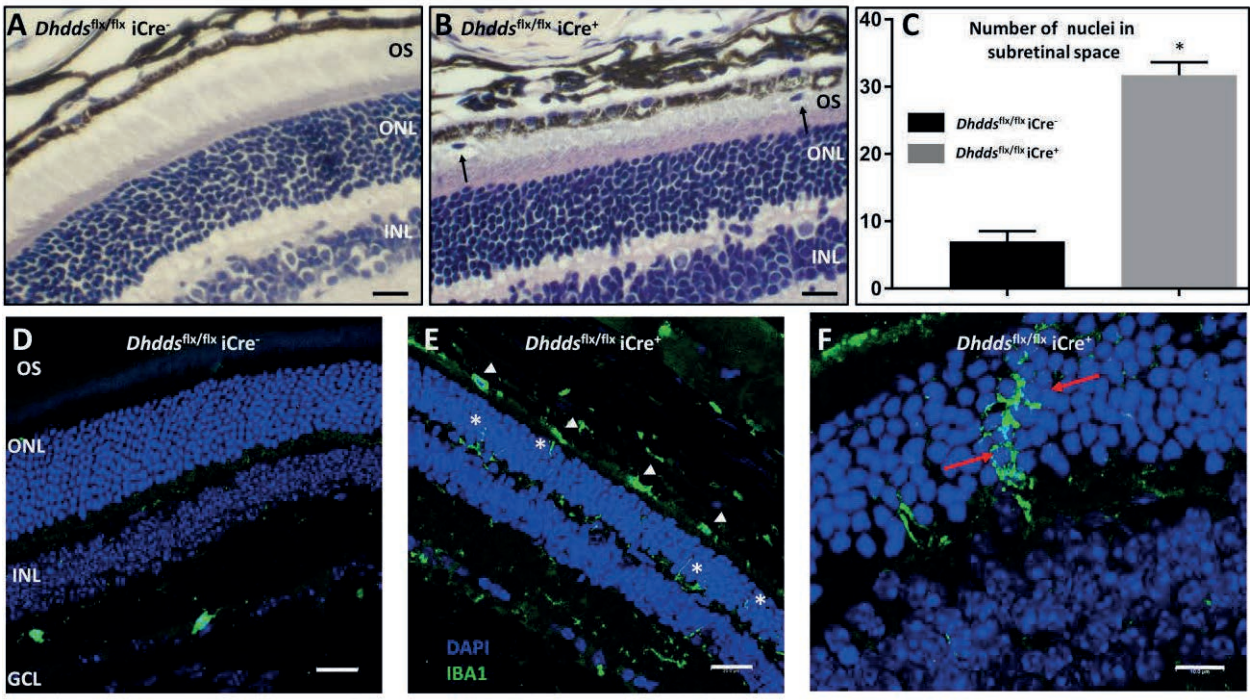

Figure S8. *Dhdds*$^{flx/flx}$ iCre^{+} retina exhibits significant increase in cells in the subretinal space. Related to Figure 4.

Further characterization of microglial infiltration and phagoptosis. **(A, B)** Histology of control and *Dhdds*$^{flx/flx}$ iCre^{+} retinas, respectively, at PN 5 weeks of age (H&E staining). Quantification of cells in the subretinal space was performed on retinal tissue sections of each genotype (8 eyes per genotype, 3 sections per eye; 10-µm thickness). This compartment of the retina normally is occupied by photoreceptor outer segments and extracellular matrix, but not other cells. However, H&E-stained cells were present in this retinal layer in *Dhdds*$^{flx/flx}$ iCre^{+} mice (**B**, *black arrows*). The same region shown in a control retina (**A,** *open bracket*) is devoid of mislocalized cells, although the far peripheral regions of control retinas were observed to contain such cells (*not shown*). (**C**) Quantitative analysis of mislocalized cells as a function of genotype; a 4-fold increase was observed in the number of such cells in *Dhdds*$^{flx/flx}$ iCre^{+} retinas, relative to controls. (**D-F**) In the young, control mouse retina, horizontally ramified, Iba-1-positive microglia were observed only in the inner retinal layers (**D**). By contrast, the *Dhdds*$^{flx/flx}$ iCre^{+} mouse retina shows microglial infiltration into the ONL (**E,** *asterisks*), as well as in the subretinal space and outer segment (OS) layer (**E,** *arrowheads*). A representative higher magnification image of a *Dhdds*$^{flx/flx}$ iCre^{+} mouse retina shows activated, Iba-1-positive microglia surrounding photoreceptor nuclei, indicative of active “phagoptosis” of live photoreceptors by microglia (**F,** *red arrows*). [Scale bars: **D**, **E,** 20 µm; **F,** 10 µm.]

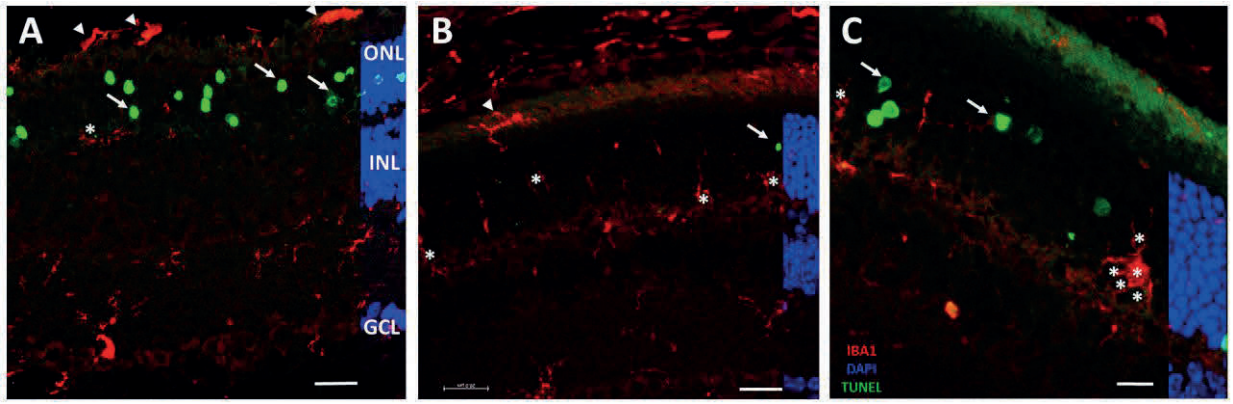

Figure S9. Cell-autonomous photoreceptor cell death and phagoptosis in *Dhdds*$^{flx/flx}$ iCre^{+} mice. Related to Figure 4.

Additional representative confocal micrographs (**A-C**) demonstrate TUNEL-positive photoreceptor cells (*white arrows*, green channel), as well as phagocytic uptake of live, TUNEL-negative photoreceptors by Iba-1-positive microglial cells (*asterisk*, red channel). Iba-1-positive microglial cells were found in the subretinal space (*white arrow head,* red channel). DAPI labeling of the nuclear layers is shown on the right-hand side of each image. [Scale bars: (**A, B**) 20 µm; (**C**) 10 µm.]

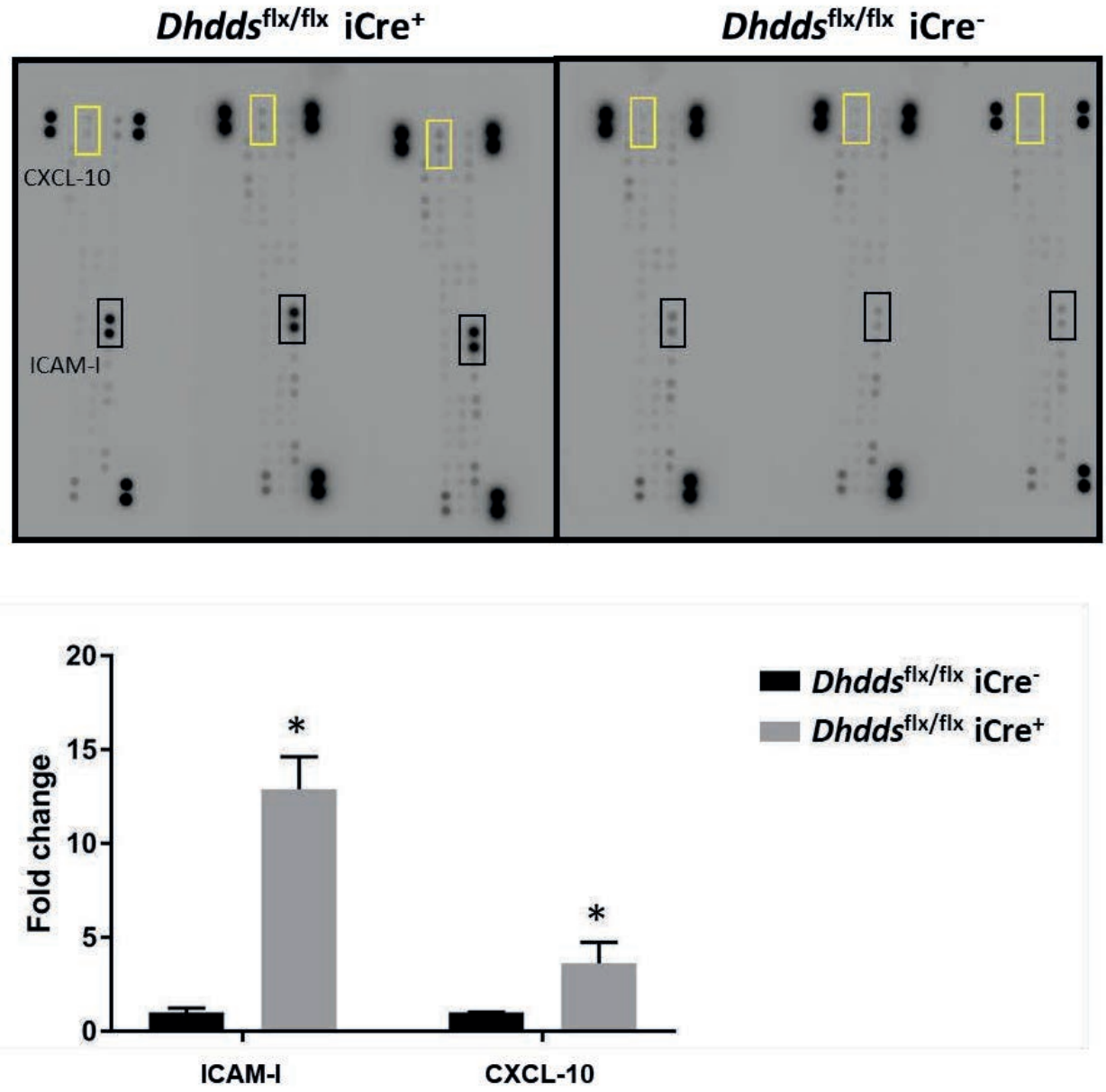

Figure S10. Sandwich ELISA-based cytokine array analysis of retinal extracts from PN 5-week old *Dhdds*$^{flx/flx}$ iCre^{+} and control mice. Related to Figure 4.
Representative ELISA assay results for the presence of selected cytokines (CXCL-10 and ICAM-1). Background-subtracted luminescence signal was measured using ImageLab® software. Significant increases in retinal ICAM-1 and CXCL-10 levels (*$p<0.01$, n=5/group) were observed in *Dhdds*$^{flx/flx}$ iCre^{+} mice, compared to controls. This is further characterization of ICAM1 upregulation as observed by Western blot analysis (see **Figure 4**).

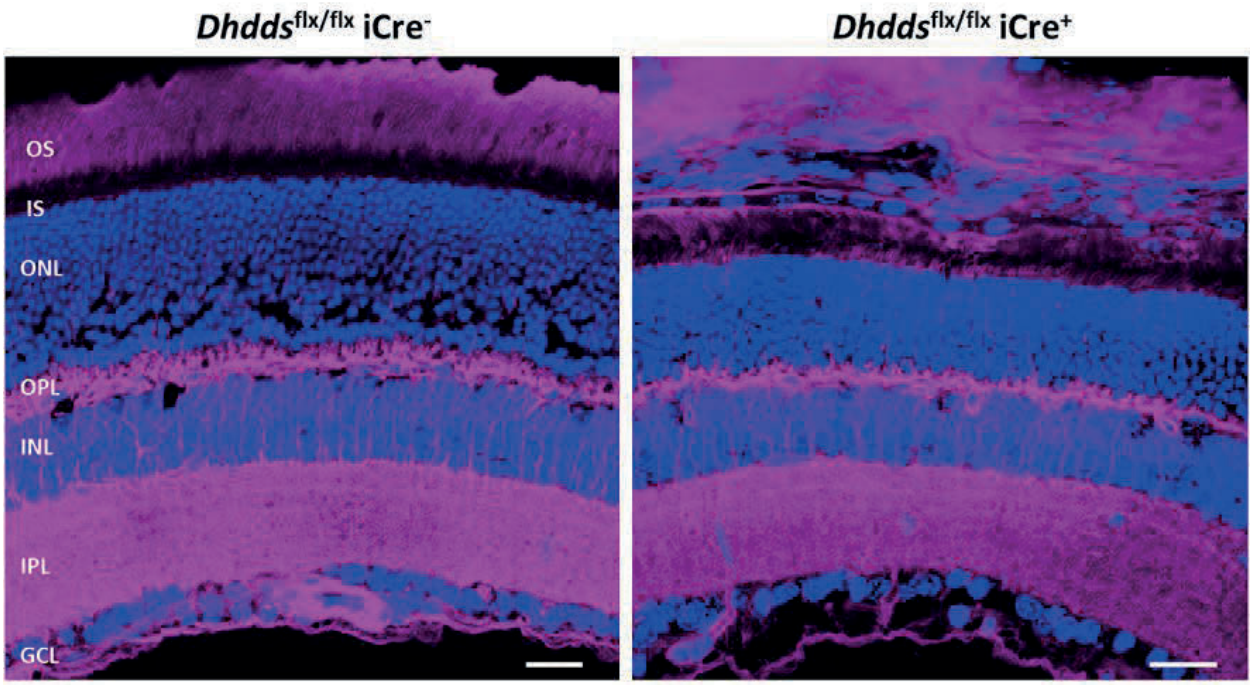

Fig. S11. Lectin cytochemistry demonstrates fluor-conjugated wheat germ agglutinin (WGA) binding to retinal photoreceptors in *Dhdds*$^{flx/flx}$ iCre^{+} mice. Related to Figure 5.
WGA (pseudocolored *magenta*) selectively binds to β-1,4-GlcNAc-containing extracellular matrix components surrounding rod, but not cone, photoreceptors as well as the extracellular matrix in the ONL. Note the comparable, robust WGA staining of retinas from PN 5-week old *Dhdds*$^{flx/flx}$ iCre^{+} (*right panel*) and control (*left panel*) mice. This is in agreement with the lack of glycosylation as observed in **Figure 5.** [Scale bar: 20 μm.]

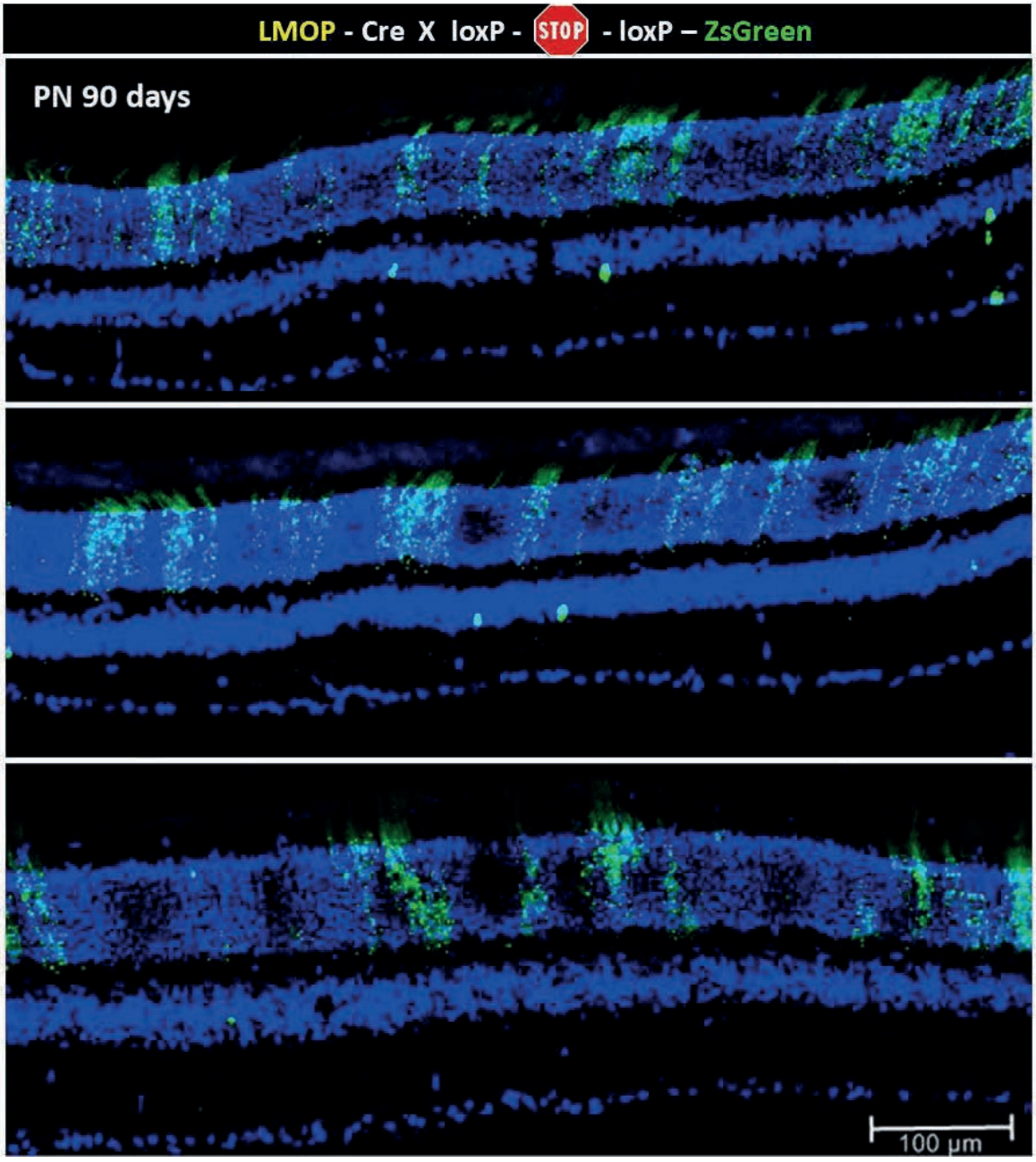

Figure S12. Mozaicism of Cre recombinase activity in the LMOP Cre mouse line. Related to Figure 2.
LMOP-Cre mice were crossed with ZsGreen reporter mice. Representative confocal microscopy images of mouse retinas (n=3, PN 3-month old) exhibit patchy expression of ZsGreen, which is inconsistent with the expected uniform distribution of rhodopsin in that layer of the mouse retina. [Scale bar: 100 µm.] Hence, for this study, we chose instead to utilize the Rho-iCre75 mouse line for generation of the rod-specific *Dhdds* knockout mouse line (*Dhdds*$^{flx/flx}$ iCre^{+}) described herein.

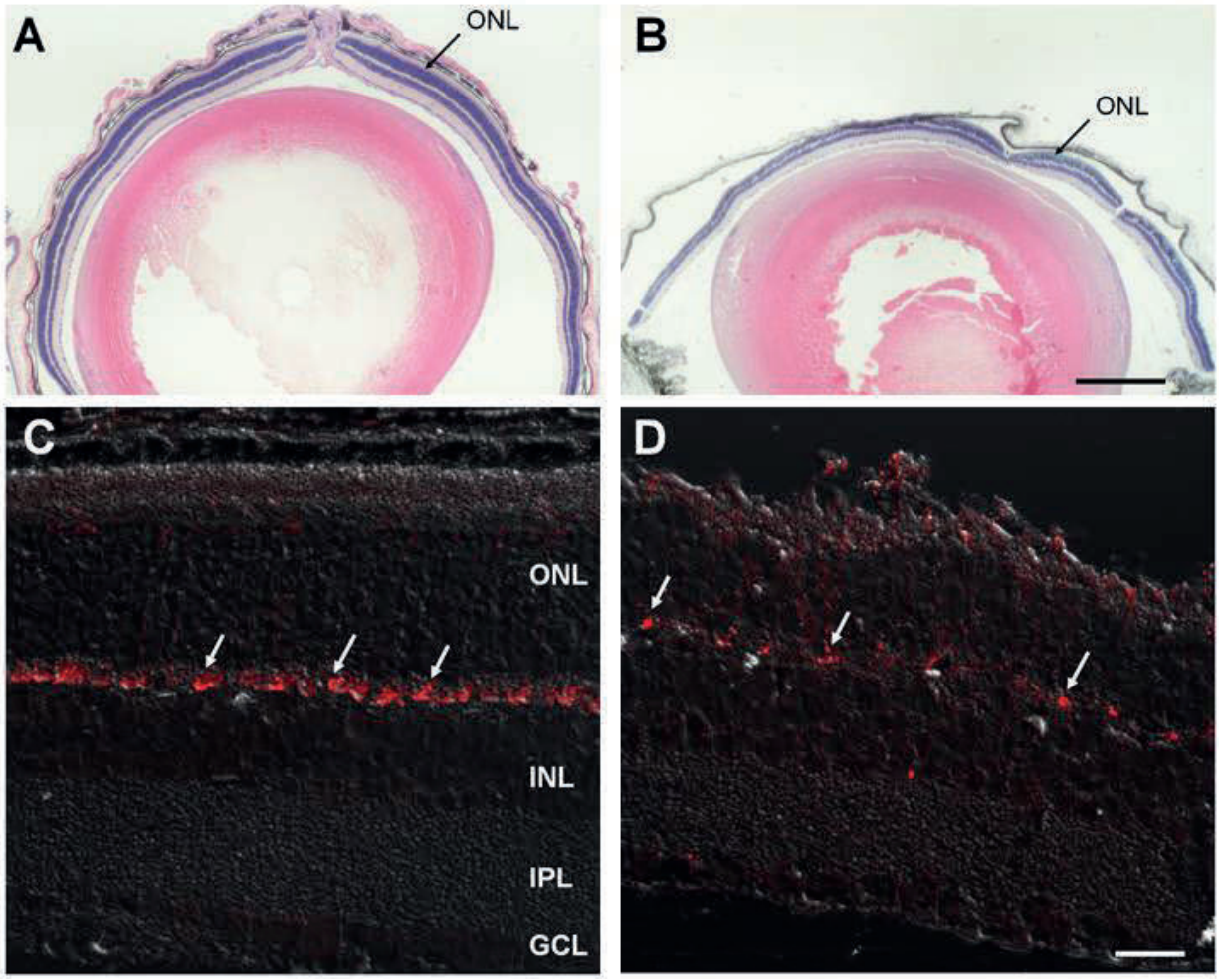

Figure S13. Low magnification image depicting retinal thinning and persistence of cone photoreceptors. Related to Figures 2 and 3.

Spectral domain optical coherence tomography (SD-OCT) imaging demonstrated significant thinning of the *Dhdds*$^{flx/flx}$ iCre^{+} retina (see **Figure 2**). Low-magnification light micrographs of H&E-stained control (**A**) and PN 5- week old *Dhdds*$^{flx/flx}$ iCre^{+} mice (**B**) also demonstrate significant thinning of the photoreceptor layer in *Dhdds*$^{flx/flx}$ iCre^{+} mice. Immunohistochemical analysis of ocular tissue sections from control (**C**) and *Dhdds*$^{flx/flx}$ iCre^{+} (**D**) mice, stained with anti- cone arrestin antibody (pseudocolor: *red*), demonstrating arrestin-positive cone synaptic termini as well as immunopositive elements in the inner and outer segment layer regions. [Scale bar: (**A,B**) 500 µm; (**C,D**) 20 µm.